Politecnico di Torino

High density, multifunctional neural probes for massively parallel read-out and control

BERKELEY LAB

MOLECULAR FOUNDRY

Master degree in Nanotechnologies for ICT's

Supervisors:
Dott. Matteo Cocuzza
Dott. Stefano Cabrini
Vittorino Lanzio

Author:
Paolo De Martino

Contents

Abstract

This thesis work, carried out at Nanofabrication facility of the Molecular Foundry, a division of the Lawrence Berkeley National Laboratory (LBNL), focuses in a Multidisciplinary project involving the optimization of several nano-fabrication processes of optical, electronical and mechanical parts of Multifunctional Optoelectronic Neural Probes aimed at high density parallel read-out and control of the central nervous system for *in-vivo* experiments in rats. The probe consists of a micro tip able to sense and stimulate the brain tissue exploiting a set of electrodes for the read out and an optical system to selectively excite neurons with high temporal and spatial resolution. This work is focused on the optimization of the design and the fabrication of the electrical layer, on the etching processes, on the stacked integration of components layers, on the electroplating of metal as well as carbon based material. The results obtained consist on the integration of an optical and an electrical layer with good performances and reproducibility. The further optimization and development of such devices will open the possibility to study neural networks with higher spatiotemporal resolution in different areas of the brain.

CHAPTER 1

Introduction and State of the Art

This chapter will be focused on a introduction on the theoretical background aimed to understand the purposes and the goals of this project. An overview on the working mechanism of neurons and on the state of the art of Neural probes will be given, in order to understand the design and fabrication choices taken.

1.1 Brain and Neurons

With around hundreds of billion of neurons connected in networks trough 100 trillion of axional connections, the human brain is today considered the most complex system known. [1] These networks are in constant state of electrical and chemical activity, thanks to which the body physiology is kept stable, and we can sense the world around us, think and talk. The brain consists of the cerebral hemispheres and the brain stem, the latter is divided into hind-brain, mid-brain, and the diencephalon. Each of these three parts have a fundamental role in the vital functions control:

the hind-brain is an extension of the spinal cord and contains neurons networks that control mainly breathing and blood pressure; each group of neurons in the mid-brain seem to use predominantly a particular type of chemical messengers transmitted up to the cerebral hemispheres and it is thought these can modulate the activity of neurons to mediate functions as sleep, attention or reward. The diencephalon instead is divided in two very different areas called the thalamus and the hypothalamus: the thalamus transmits impulses from the sensory system to the cerebral cortex, which in turns replies sending signals back to the thalamus.

The cerebral hemispheres consist of a core, the basal ganglia, and an extended but thin surrounding sheet of neurons making up the grey matter of the cerebral cortex. Packed into a limited space, the cerebral cortex is folded up and weaves around the skull to enable a much larger effective surface area. This cortical tissue is the most highly developed area of the human brain, it is divided into a large number of discrete areas, distinguishable in terms of its layers and connection. The functions of many of these areas are known, as the voluntary actions, language, speech and higher functions such as thinking and remembering. However the study of the functions of the cerebral cortex is still one of the most exciting and active areas of research in neuroscience. [2]

The structure and function of the brain are most appropriately understood, for our purpose, from the perspective of their highly specialized cells: the *neurons*, the interconnected, highly differentiated, bioelectrically driven, cellular units of the nervous system. [1] Moreover Neurons are classified in many different ways, according to their functions, the transmitter they synthesize, and their shape. Their general shape and, in particular, the number of extensions form the cell body are very important in the determination on the way they are interconnected with the surroundings neurons.[1]

1.1.1 Structure of a Neuron

The neuron, shown in fig.1.1, is composed by dendrites, a cell body, an axon and synaptic terminals (axon terminals). This structure can be analysed from a functional subdivision into receiving, integrating and transmitting components. Roughly speaking, the dendrites receive, the cell body integrates and the axon transmits, trough a process called polarization.[2]

The dendrites, or dendritic trees, are tree shaped extension with their trunks directed toward the cell body in order to maximize the input signals that the neurons can receive. Once the signals arrive to the cell body, from the nucleus, placed inside, an electrical impulse starts, called action potential, which travels through the axon.

The axon (outgoing channel of a neuron) carries information away from the cell body toward its output terminals. Once the signal arrives to the axon terminals it is transmitted trough the

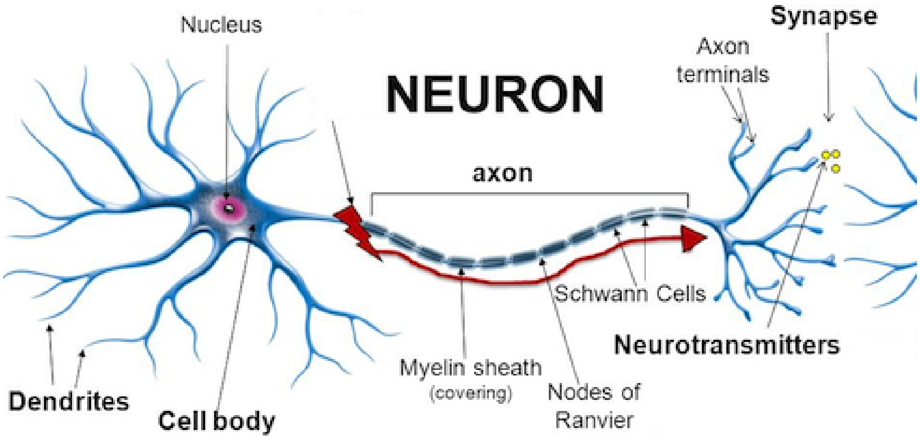

Figure 1.1: Typical nerve cell, or neuron, structure. Credit [3]

synapse. The synapses are regions where the axon contacts the dendrites of other neurons and can be either chemical (release of neurotrasmitters) or electrical in nature.[4]

Therefore all neurons' physiological activity is both electrical and chemical. Once stated the neuron receives the information from multiple synapses by the dendrites in form of chemical signals, they are then transformed into electrical signals (ionic currents) that are added or subtracted to the other coming from all the other synapses. [2]

In order to understand how to monitor and control the activity of a neuron the working principle of the electrical transmission of information carried by the axon, the role of the Cell membrane and of the Intrinsic membrane proteins deserve a deeper explanation.

1.1.2 Action Potential

The membrane of the nerve cell is surrounded by an extracellular and an intracellular fluid containing ions at different concentrations and it is semipermeable to some Ions (Na^+ and K^+ in particular). There is a greater concentration of sodium ions, Na^+, outside the cell and potassium ions, K^+, inside, in order to maintain the different concentrations the cell have to spend energy. A steady state condition can be defined, for a non-signaling neuron, when the existence of the two fluid with different concentrations of Ions separated by the cellular membrane generates an equilibrium potential difference across them. The latter is called "resting potential", it is conventionally measured considering the outside solution as ground and his value is around $-70mV$. During this condition because of the gradient of concentration there would be a constant leak of K^+ ions toward the outside of the cell and a leak of Na^+ toward the inside, this diffusive flow is balanced by the effect of Sodium-Potassium pumps (intrinsic membrane proteins) able to push the ions to maintain the gradient concentration exploiting the energy released by the hydrolysis of ATP. Then thanks to the presence of other intrinsic membrane proteins, triggered by changes in transmembrane voltage called Voltage gated channel, if the potential inside the cell changes to a certain threshold these particular channels are able to control the flow of ions. Na^+ gated channels typically open for a potential around $-55mV$ and close for a value around $+40mV$, and the K^+ channels open if the potential gets lower then around $-80mV$ and close at $+40mV$. [4]

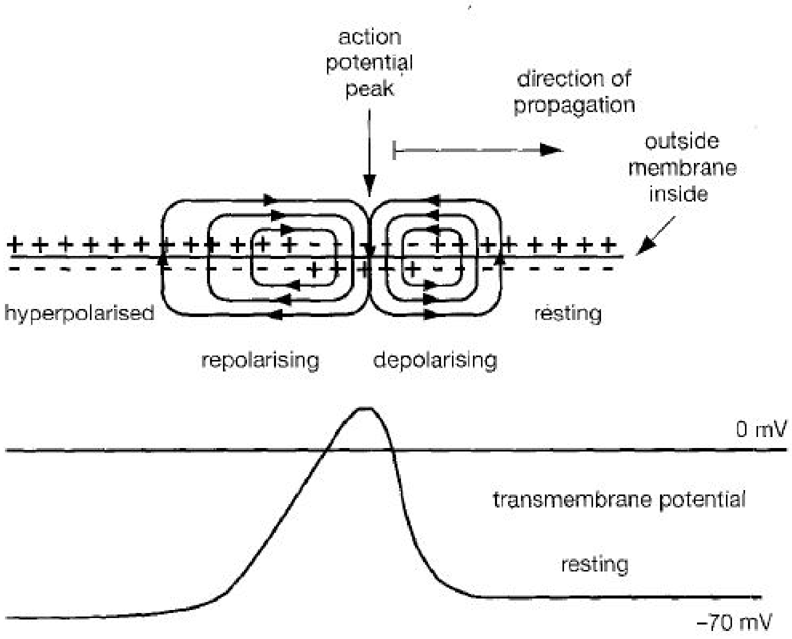

Figure 1.2: Schematic representation of the Action Potential. Credit [5]

Therefore when the potential inside the cell increase, due to an injection of positive charge in one end of an axon, it may overcome the Na^+ channel threshold opening it, typically $+15mV$, giving rise to the so called "Action Potential". In this case sodium ions will flow into the cell thanks to both the concentration and the electrical gradients increasing more the potential in that point, leading to a rising of the potential up to the threshold also in adjacent portion of the membrane. This mechanism let the "depolarization" to spread . The potential will keep raising until the $40mV$ threshold is reached, at this point the Na^+ channel close and K^+ channel will open letting potassium ions going out the cell (polarization). Then the potential will drop until the $-80mV$ threshold, where the potassium channel are closed and the potential will come back to the resting value of $-70mV$. This mechanism gives rise to the intracellular active potential spike, in fig. 1.2. [5] When the Na^+ channels are closed, additional depolarizing stimuli will not lead to further action potential, "refractory period": this is why the spike, and consequently the information, propagates in only one direction. [6] Moreover the process allows the electrical perturbation on the membrane to be restored every time an adjacent voltage gated channel is activated, and so it lets to the pulse travelling across the axon to not loose its amplitude.

1.1.3 Synapses

Once the action potential, after it has travelled trough the whole axon, reaches its terminal where there is a gap between the nerve ending and the dendritic spine of the next cell, the electrical currents responsible for the action potential can't overcome the gap. The latter region is the called Synapse, it consists of a presynaptic nerve ending in the axon, a small gap, and the postsynaptic component.

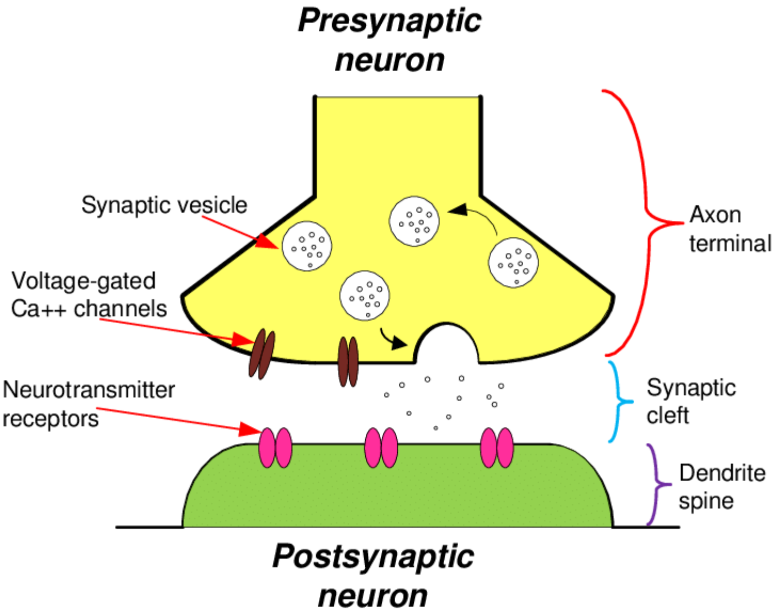

Figure 1.3: Representation of a chemical synapses. Credit [7]

Chemical synapse In chemical synapses the information transit across the gap is accomplished by chemical messengers called neurotransmitters. At the end of the axon, in small vesicles, neurotransmitters are stored. The arrival of the action potential leads the entering of calcium (Ca^{++}), opening the respective ion channels, that activates enzymes acting on presynaptic proteins responsible of the fusion of the vesicles with the cell membrane with the consequent release of the chemical messengers. Trough a diffusion mechanism the neurotransmitters are able to cross the gap, called synaptic cleft and with a dimension of around $20nm$. Once arrived in the dendritic spine they interact with synaptic receptors placed in the membrane of the next neuron, as shown in fig. 1.3. This interaction generally causes the opening of an

Ion channel, for the Ionotropic receptors, causing the previously explained cascade of signal in the membrane's channel, the action potential. [2]

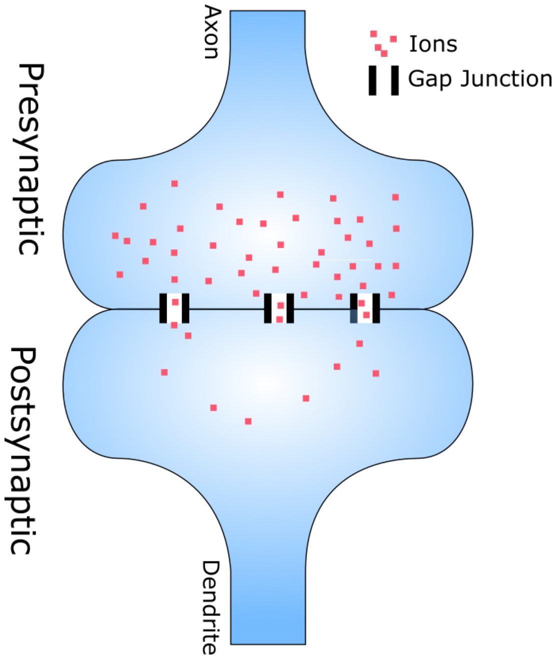

Figure 1.4: Schematic representation of an electrical synapse. Credit [8]

Electrical synapse Thanks to the continuous research that have been done in the neuroscience field, it has been evident that neurons communicate with direct electrical connections as well. In this case the ionic currents can flow straight out from one neuron to the next one through channels, called gap junctions, as shown in fig. 1.4. [4]

1.2 Brain Devices and state of the art

In the following a motivation, based on the researches and on the technological developments carried out in the last decades, about the rising of studies on neural probes will be given.

From the early beginning of the new century, in first sixteen years the numbers of death due to neurological conditions as Alzheimer, Parkinson, Epilepsy and other neurological diseases, has more than double from $1,053,170$ to $2,342,560$ death estimated according the World Health Organization [9]. This has raised the interest in the development of new technologies and strategies with the purpose to investigate the central Nervous system. Moreover the new advances in the field of rehabilitation and medical care for paralyzed patients in the area of neural prosthetics or orthotics, in order to restore function lost due to damage to nervous system, have gained an increasingly large interest. [5] The main idea is to exploit a device able to sense and/or stimulate the electrical activity of neurons.

1.2.1 Invasives vs Non-Invasives

Current techniques to record the action potential of nervous cells range from single neurons up to sensing superimposed neural activity of large population of neurons. These techniques vary in spatial and temporal resolution and invasiveness. The lowest spatially resolved information can be obtained non-invasively using Electroencephalography (EEG) on the scalp or Magnetoencephalography (MEG), both reflects the activity of large neuronal populations. Similar signals, going at higher spatial resolution as shown in fig. 1.5, can be recorded trough regular grids or stripes of electrodes implanted subdurally on the surface of the cortex, this invasive technique, called Electrocorticogram (ECoG), reflects synaptic inputs of the neuronal population beneath each electrode.

Increasing the invasiveness as well as the resolution, implanting microelectrode arrays into the cortex enables the possibility to record the extracellular potential capturing spike signals and local field potential in the vicinity of the electrode tip. From these strategies three kind of signals can be derived: Local Field Potential (LPFs), Multi unit activity (MUA) and Single unit activity (SUA). LFPs, as the previous techniques, give back analog signals, and they are extracted by low-pass filtering ($<$ca. $300Hz$). Instead SUA and MUA measure spiking activity of discrete events in time, they are obtained by high-pass filtering of the extracellular potential ($>$ca. $300Hz$) with the difference that the first one are processed with spike detection and spike sorting mechanism, assigning each spike to its corresponding neuron, and the second one is not processed so the signal is made of spikes originating from multiple neurons. [10]

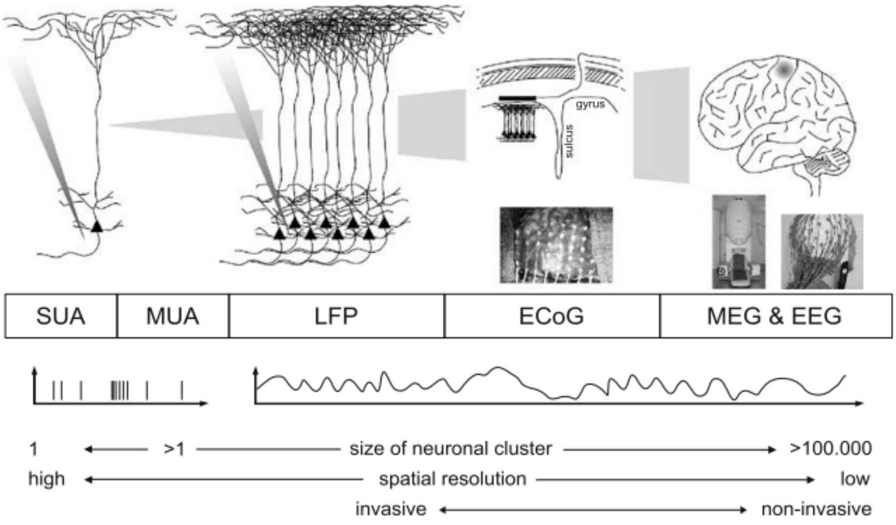

Figure 1.5: Schematic overview of the recording techniques. Credit: [10]

Therefore despite having a common source, there are mainly three differences between invasive and non-invasive signals that can be underlined. First of all the number and type of neurons: since the electric field produced by neurons decay exponentially with distance, the number of superimposed fields produced in a confined area of simultaneously active neurons is, for example, magnitudes smaller for LFP than EEG. Hence with EEG the activity of small neuronal clusters have a lower Signal-Noise Ratio (SNR), and so almost undetectable. In addiction EEG signals are composed for the great part by fields coming from pyramidal neurons, since their morphology and their high presence in the cortex allow to fields to add up and reach the scalp. Second, the signal composition: tissue acts as a low-pass filter attenuating high-frequencies signal components, therefore non-invasive recording allow just low-frequency activity analysis ($<\approx 90Hz$).

Instead invasive recording techniques convey information up to several KHz. Third, spatial distortion: since the extracellular space is composed with media having different electrophysiological properties, this influences how fields spread. Moreover the celebrospinal fluid, skull, and scalp add further spatial distortion before reaching an EEG electrode. These limitation are intrinsic in non-invasive techniques and can not be overcome, but however the latters allow to monitor large-scale neuronal activity of the entire brain at low cost and risk-free, vice versa invasive recordings can be deeper and can cover an higher frequencies range high with higher spatial and temporal resolution being more localized and more laborious. [11]

In general, it seems that non-invasive recording techniques, such as Encephalography (EEG), allow gross measurements of the brain electrical activity: in order to enable detailed studies of individual neurons, for basic neuroscience, and to ensure an higher control of prosthetic devices, in the field of Brain Machine Interface (BMI), advances have been made to provide high selective invasive transducers with ideally one-to-one site-to-neuron correspondence. To achieve this goal two areas of science have been working together in last decades: Neuroscience and Nanotechnology. [5]

1.2.2 Devices state of the art

As previously said in order to satisfy certain properties, as high resolution and high SNR ratio, devices acting as neural transducers to detect changes in the electrical potential associated with active neurons and to stimulate an activity sending a current through the tissue have been studied. One of the first device thought for detailed studies on single neurons is glass microelectrode, back in $1920s$. [5] These microelectrodes were made of glass capillary tube with a very fine tip, $< 2\mu m$ in diameter, filled with an electrolyte solution. When tip is brought in contact with a nervous cell membrane, the application of pressure can break the membrane providing an electrical measurement from the interior part of the cell respect a reference electrode outside the cell. Around $1950s$, the first metal wire microelectrodes were fabricated. They consisted in a metal (usually tugsten) wire electrolytically etched and then insulated up to the tip. These techniques are able to record an extrtracellular signal. In general these kind of devices had some limitations: it was difficult the insertion of a large number (> 30) of them in a small volume of tissue, complications in long-term experiments on freely moving animals, and they were usually hand-made by so the reproducibility of the device in terms of dimensions and electrical characteristics of the tip was very low. [5] The development of microelectronics technologies gave the possibility to overcome the hand-made and scalability fabrication problems improving accuracy and repeatability with the introduction of silicon-based microprobes to interface neural tissues. The first device of this family was proposed by Wise et al. [12] in 1970s. It was made of an array of gold electrodes, on a silicon carrier, covered with $0.4\mu m$ of silicon dioxide then selectively removed at tips using photograving techniques in the recording areas for extracellular signals.

Nowadays micromachining technologies enable the fabrication of devices with submicron features, however micromachined microelectrode devices seems to be limited in the availability of device technology, supporting technology and practical expertise. In addition to these devices aimed to establish a neural-electrical interface, another aspect is necessary to be taken into account: the role of neurochemical signals in synapses, which is gaining interest since several brain disorders are attributed to their disturbed balance.[13] Neural-chemical interfaces monitor and modulate neurons activity by detecting neuro-chemical, such as neurotransmitters, and by delivering chemical therapeutic elements. More recently, polymeric microprobes have reached high interest thanks to their simple fabrication process, their flexibility and biocompatibility.[14, 15, 16, 17]. For example, developed polyimide based neural probes are flexible and mechanically resistant with electrodes in both side or microtank and microchannels for targeted drug delivery.

1.2.3 Neural Probes State of the art

As discussed before invasive device have some advantages in cases requiring a one-to-one interface with neuron ensuring high signal quality. Moreover thanks to the rapid development of microelectronics fabrication technologies, devices that minimize the invasiveness, in dimension also with the use of biocompatible materials, have reached popularity. The most popular invasive technique is based on the application of multielectrode devices penetrating in the brain cortex. [13] The progression of silicon based devices allowed the development of two main approaches, on the device general structure, based on the fabrication point of view: out-of-plane Utah-type and in-plane Michigan-type.

- **Utah-style** pillars array have proven their potential in neural activity recording even in human experiments. Bhandari et. al. [18] described the novel fabrication concept of Utah electrodes: the arrays are micromachined from a thick ($> 1mm$) silicon substrate. electrode columns are formed by dicing of a grid, further wet chemical etching provides smooth pillars and sharpened probe tips. The metallization is performed usually with a lift-off process, then they are electrically isolated by deposition in LPCVD, and finally the tips are released or deinsulated in O_2 plasma exploiting a photoresist mask. Their use is limited due to the fabrication process itslef, since probe length is limited by the thickness of the wafer; therefore application are restricted on cortical studies.[18] An example is shown in fig. 1.6

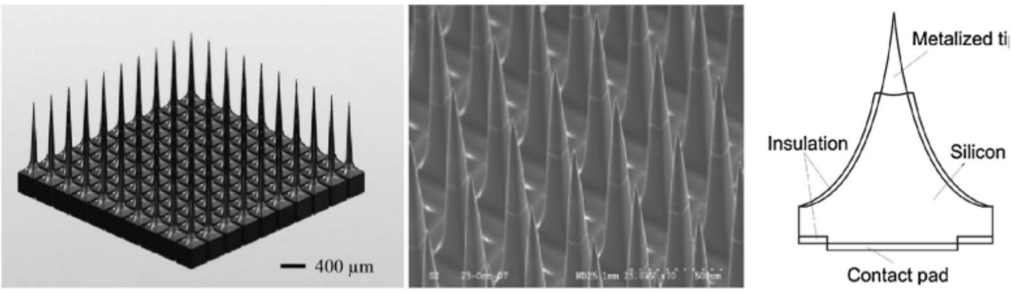

Figure 1.6: Utah-style probe with representative SEM images and a cross-sectional schematics. Credit [13]

- **Michigan-style** planar microelectrode arrays, istead, can benefit more from the recent developments in semiconductor industry. Conventionally their micromachining is based on thin film deposition and patterning of the deposited layers by photolithographic techniques to define recording sites, leads and bonding pads in order to interface both neural tissue and external signal processing units. Michigan probes have been successfully used in several neuroscience applications, also if they still suffer from some disadvantages related to limited thickness ($> 15\mu m$) and length ($> 8mm$), but at the same time their fragile geometry is advantageous because of reduced cell damage during insertion.[13] An example is shown in fig. 1.7.

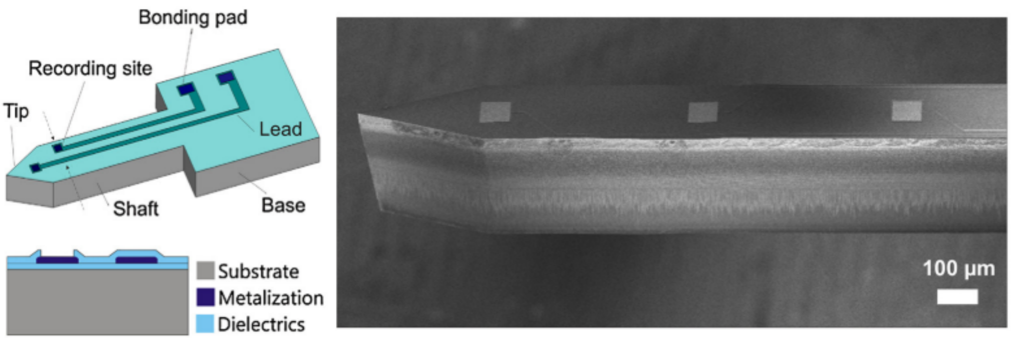

Figure 1.7: Michigan-style probe with representative SEM images and a cross-sectional schematics. Credit [13]

In order to meet the biocompatibility demand, the implanted microelectrodes should not cause toxic or immunologic reaction, should not destroy or compress adjacent cells or tissues and should be stable in long term without encapsulation. It is possible to influence the electrodes design and implantation parameters to reduce the mechanical impact, which is one of the most dominant reason for short term immune response. Moreover micro and nanoscale modification of surface properties can contribute in an efficient way to delay or control the immune response of the surrounding tissue.

In a macroscopic view neural tissue is exposed to considerable mechanical impact when the probe is inserted. The magnitude of such impact depends from different parameters such as the geometrical properties of the probe, the electrode configuration and the circumstances of the surgery. The traumatic brain injury (TBI) should be avoided, minimizing the brain tissue compression, because it eventually results in cell death due to the cortical layers blood circulation disorder caused. The compression can be quantified by the tissue dimpling value, it is defined as the depth covered by the probe tip from touching the tissue until the penetration moment. The probe as well should withstand the axial force (penetration force) exerted during the insertion into the brain tissue. The buckling force, of specific electrodes designs, can be predicted applying the Euler-Bernoulli beam theory, it is a very important parameter to be taken into account since it is one of the fundamental failure modes during microelectrode implantation; therefore devices should be designed such a way this value well exceed the range of penetration forces.

On the other hand, in a mirco- and nanoscale point of view long term signal recording in chronic experiments is currently limited since an immune reaction starts surrounding the probe, view as a foreign body, with the so-called glial scar. As a result the electrical coupling between the recording sites and the extracellular space is gradually changing because of the isolation performed by the glial sheath. Surface modification techniques is one of the best strategies to delay the above mechanism. The effect of texturing the substrate material, trough a wide variety of etching processes, has been investigated by exposing nanostructures Si surfaces to several type of neural cell culture. These studies revealed that nanoscale roughness is advantageous in promoting cell adhesion, and reduction of immune response. [13]

In 2002, Norlin et al. [19] were able to develop a 32-site neural recording probe with multiple shanks. Starting form a Silicon-On-Insulator substrate the shanks were released by a double-sided deep reactive etching using the SiO_2 layer as etching stop. On top of these shafts, of dimension $5mm \times 25\mu m \times 20\mu m$, by e-beam evaporation Au conductor traces were created, ending in $100\mu m^2$ Ir electrodes. The interconnect and packaging solution, based on flexible printed circuitry, provides a well adapted devices to the requirements of neuroscientists. [19] However, the trend in the last years is following the scaling of probe design in order to increase the number of recording sites and develop a complete system for neural recordings. In 2011 Stevenson and Kording [20] firstly stated that the number of simultaneously recorded neurons approximately doubles every 7 years, following similarly the Moore's law for the exponential growth of numbers of transistors in integrated circuit. The delay, respect the advances in integrated system technologies, have to be found in a lack of similar economic drives and industrial support together with some technological step to be overcame in scaling sown process, like cross-talk, electrode impedance and thermal noise. [21] Despite this, many type of probes have been introduced with the possibility to establish more precise computational models of neural networks, combining deep-brain optical imaging and high-density electrophysiology. [13]

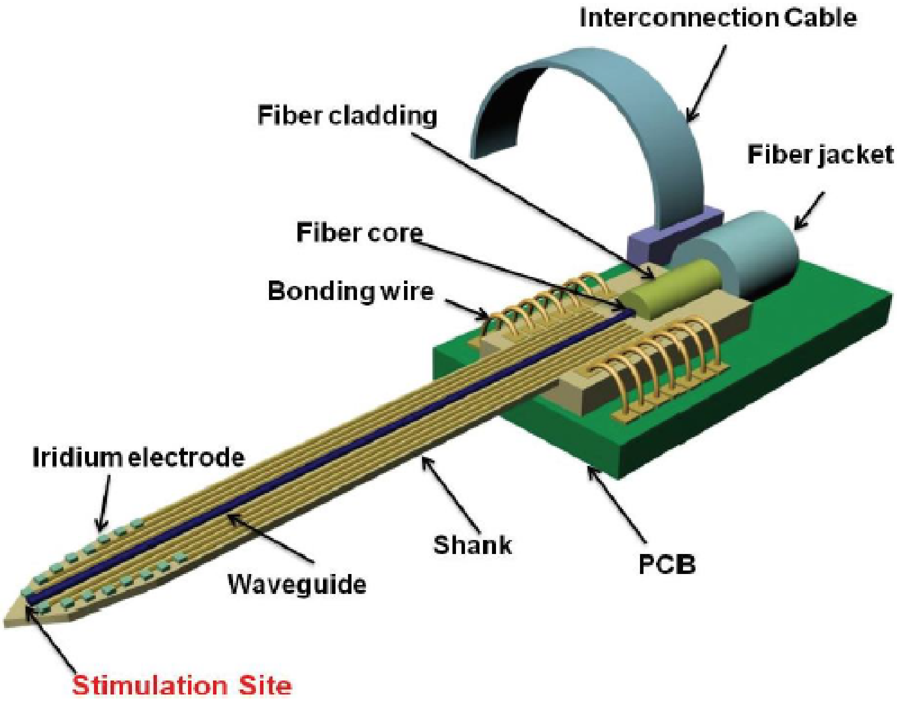

Figure 1.8: Schematic of probe with Electrical recording site and integrated waveguide for optical stimulation, proposed by Cho et. al.[22]

For example Cho et. al. [22] in 2010 proposed a 16-site neural probe integrated with a waveguide for optical stimulation. This device have been designed in order to selectively stimulate target neurons trough the light from an integrated waveguide and also monitor extracellular neural signals thanks to the recording sites. The probe proposed by Cho is shown in fig. 1.8

The optical waveguide is composed of a SU-8 core and an oxide cladding, an U-groove has been created on the silicon substrate to ensure a correct alignment with an external optical fiber. The fabrication process of the device have been modified from a standard Michigan approach in order to integrate a bottom cladding layer under the waveguide core. [22] The 16 Ir electrodes are placed close to the light spot to monitor extracellular signals during the optical stimulation. The total thickness of the shank is actually maintained below $20\mu m$ in order to not induce any additional cell damage during implantation. [22]

The last device was an example of how in the last years probes with several integrated investigation elements have been designed and fabricated. The ability to both stimulate and record the electrical signals in neurons with a single device, called "Multifunctionality", has been a central point for implanted devices over a decade. [23] The main three approaches, with which the monitor and the modulation of neural activities can be carried out, are: Electrical, Optical and Chemical. The combination of the three constitutes a complete interface between the device and the neural tissue. Although the blood-brain barrier makes the development of pharmaceutical treatments for brain disorders difficult. The blood-brain barrier is an high selectively semipermeable border in the brain blood vessels, made of specialised endothelial cells. [2] Even though the difficulties in interacting chemically with neural activities, some probes are also equipped with an on-chip feedback and control of local drug delivery, as demonstrated by Li et al. [24] and Papageorgiou [25]. Multifunctionality in probes development promises the ability to monitor the neural tissue and to respond with an appropriate pharmaceutical or therapy in real time, this particular approach is known as "Closed-loop control".

[23] However the real challenge is to to integrate more than one of these modalities in a small volume, to ensure multiple functionalities without sacrificing spatial or temporal resolution and to minimize the chronic immune response.

Another limitation to be taken into account is the fabrication compatibility of different monitor or control modalities in the same device. In order to investigate this point, in the following an overview of two strategies used in neuroscience is carried out.

1.3 Electrophysiology and Optogenetics

1.3.1 Electrophysiology

Electrical Interfaces have been adopted extensively in neuroscience as tools to study neural Electrophysiology. This field is known as the "gold standard" for the investigation of neural signaling, and it embraces all the manifestations of the nervous system functions, from the molecular to higher level activities, such as cognition and behavior. [13, 26] The link between the nervous system and the electrical activity was already discovered by Galvani 200 years ago. Electrophysiology allows to read directly the neurons activity with an extremely high signal-to-noise ratio exploiting metal, glass or silicon electrodes that are able to record electrical signals coming from ion fluxes across electrogenic cell membrane. [26] Moreover the key point of electrophysiology is the ability to record directly the electrical activity, without the need to trans-form it into a different signal. This is, at the same time, its weakness since in order to have an electrical access to the nervous system a physical contact with the tissue is required. [26] Electrical interfaces, such as patch clamp devices, have been studied, they typically consist of electrodes in contact with nervous cells that modulate their surrounding ionic environment (via action potential) giving rise to collective ionic variation which can be transduced into electrical signals via the electrodes. [23] The resulting interface can be modelized with an equivalent electrical circuit shown in fig. 1.9. When action potentials propagate through a neuron, as already explained, the opening of ion channels in the membrane creates a local imbalance of charge. [23] This generates the already cited Local Field Potential, in the figure e_n, that is then transduced by the neural-electrical interface.

The interface can be described with:

- R_e: Electrode material resistance;
- C_e: Electrode double-layer capacitance;
- R_{seal}: seal resistance;

then the biological fluids and the electronics:

- R_s: Physiological buffer resistance;
- R_m: Metal (trace) resistance;
- C_s: shunt capacitance;
- Z_a: Amplifier impedance;

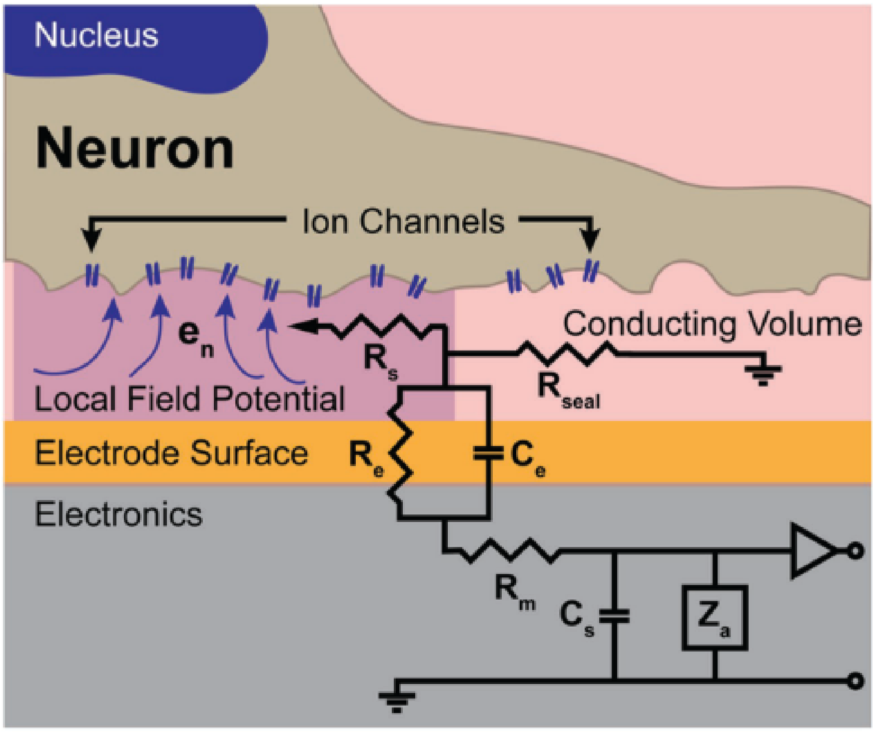

Figure 1.9: Schematic representation of a neural electrical interface. Credit: [23]

and if the system is well-designed the latters can be typically neglected.[23] One of the big limit of planar electrodes arrays has been minimize the electrode impedance to obtain a high enough signal-to-noise ratio, specially when dealing with their scaling down. The impedance:

$$Z_e = R_e + \frac{1}{j\omega C_e} \tag{1.1}$$

results to be high for reduced electrode surface area, since $C_e \propto A_{electrode}$. [23] In order to solve this problem nanostructured material have been widely used to cover the electrode, since nanostructured materials have an higher effective surface area the electrode capacitance will increase thus reducing the electrode impedance Z_e. In 1980 the first report exploiting this technique appeared, using electrochemical platinum deposition onto gold electrodes leading to a gain in signal-to-noise ratio. [23] Nanostructured platinum has features ranging from 10s to 100s of nanometers, commonly know as Black Platinum, and it presents poor mechanical stability. This is why material with higher mechanical stability such as iridium oxide, titanium nitride or nanostructured gold have been introduced. [23] However, facing the small surface area does not eliminate all the problems. In fact one of the main hurdle to overcome in electrical monitoring is the already cited foreign body reaction after implantation: local inflammatory response leads to a coverage of the electrodes by astrocytes that deposit an extracellular matrix to create a protective barrier that screens the signals coming from the neurons. In order to solve this problem, there are promising results utilizing nanostructures to directly control the adhesion of neural cells over the material surfaces. Conductive polymers (PEDOT) have also received attention thanks to their ability to form stable layers through electrochemical deposition. [23] Then, it is straightforward that the noise sources are essentially instrumental and the SNR has been maximed by the use of low-noise headstages and amplifiers, as well as the gigaohm seal of the patch-clamp technique, that allow to resolve the opening of a single ion channel. [26].

As previously discussed, the extracellular spike amplitude decreases rapidly as function of distance, however thanks to an high number or recording sites a large number of neurons can be sensed in parallel and moreover two o more recording sites allow for the triangulation of the neuron. [21]

However, in vivo electrophysiology alone is not able to link specific cell types, therefore defining genetically modified cells and combining electrophysiology recordings with optogenetics has became an important techonolgigal integration: for exaple, optogenetic stimulation of specific cell type during multiunit extracelullar recording make the determination of circuit physiology effects feasible. [23]

1.3.2 Optogenetics

Optogentic has become a powerful tool for neuroscience in the study of neural tissue. It consist in the use of light to control neural cells that have been previously genetically modified in order to express light-sensitive ion channels. [23] It can be exploited for both monitoring and modulating the neural tissue. In first case, the use of light prevents the need of a direct physical contact with the tissue, because light can travel through biological tissue. This could even replace electrodes in electrophysiology. [23] Light does not interfere with neural functions and its application leads to several advantages: high spatial resolution, with the possibility to resolve even the smallest neural structure; simultaneous measurement from a wide range of spatial locations; and most of all the access to specific cells subtypes and subcellular domains. When investigating neural functions using light a reporter must be used, which typically is a molecule that converts the meembrane potential into an optical signal. This gives an indirect optical measurement, and therefore an accurate calibration is required for a quantitative measurement. [23] In imaging the measured signal, the photon flux, come from the conversion of the electrical signal into photons and it is normally observed as a change in fluorescence.

On the other hand Optogentic can be exploited for optical modulation, it is dictated by the genetic expression of light-activated transmembrane ion channels (opsins) in targeted neural cells. It allows to the optical stimulus to selectively modulate the neural activity of specific sub-population of defined neurons, genetically modified. [23] During this technique the neural interface should deliver light at the sub-population of neurons at the minimum required irradiance. Light-activated ion channels generally respond strongly to visible light, then within a few hundreds of micrometers scattering effects through the neural tissue become increasingly significant togheter with substantial attenuation of the stimulus. A solution could be exploiting longer wavelengths to perform two photon stimulation, increasing the penetration depth, thus it would reduce the absorption volume but single channel conductance of individual opsins is generally low and has fast kinetics, so multiple opsins in a larger volume need to be stimulated nearly simultaneously to induce an action potential. [23] The use of commercial optical fibers coupled to external light is often exploited, however they have some drawbacks: their fragility, restrict movements, not possible to perform multi-site stimulation and they are not compatible with microfabrication techniques. Instead, microscale waveguides can be easily integrated with microfabrication techniques and can be coupled with external light source. They can fabricated using oxynitride of SU8 ans then can be multiplexed into Michigan or Utah style probe. [23] Other solutions consist to deliver optical stimulation through the direct implantation of micro-LED of Gallium Nitride on a sapphire substrate: they can be designed in a variety of geometries to improve spatial resolution and to modulate a large volume. But, LEDs have to be placed in proximity of the target cells and, moreover, the thermal management of the device can be an issue for the thermal fluctuations around the micro-LED, providing a non stable stimulation wavelength. [23]

CHAPTER 2

Neural Probe at the Molecular Foundry

In this chapter a detailed description of the Neural Probe designed and developed at the Molecular Foundry will be given, with a special interest at the purposes and goals of the device, following a step by step description of the existing fabrication processes [33], the improvements and the optimizations developed in this thesis work.

2.1 General Description

The purpose of this project is the study and the understanding of the communication dynamics between different layers of nerve cells in the cerebral cortex at single neuron level. These intentions have driven the work toward choices of design and materials focused on the minimal brain damage, biocompatibility, and high density of recorded cells. In order to achieve these goals a thin device able to penetrate the brain tissue, to stimulate genetically modified neurons at a certain wavelength and to record

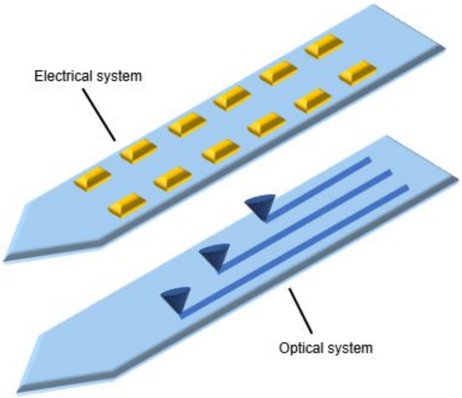

Figure 2.1: Stacked layers representation: Optical layer, with waveguide, ring resonator and focusing grating in the bottom, Electrical layer on top.

the action potentials have been designed. The solution found is the developing of a Michigan Style device.

With respect the big variety of these kind of devices present in literature, the step forward of this project is to push the limit of the existing technology to increase the integration complexity of neural probes, hence consistently increasing the population of neurons that can be studied in one single experiment exploiting Electrophysiology and Optogentics as main strategies in the investigation of the brain.

The implementation of the two latter investigation approaches have been carried out integrating them in two stacked layers of the device: the optical components as waveguides, ring resonator and focusing grating, bottom layer, and the electrical circuitry made of gold wires and electrodes, top layer, as shown in fig.2.1. This solution have been chosen in order to achieve the multifunctionality, hence the possibility to both stimulate and record, in a

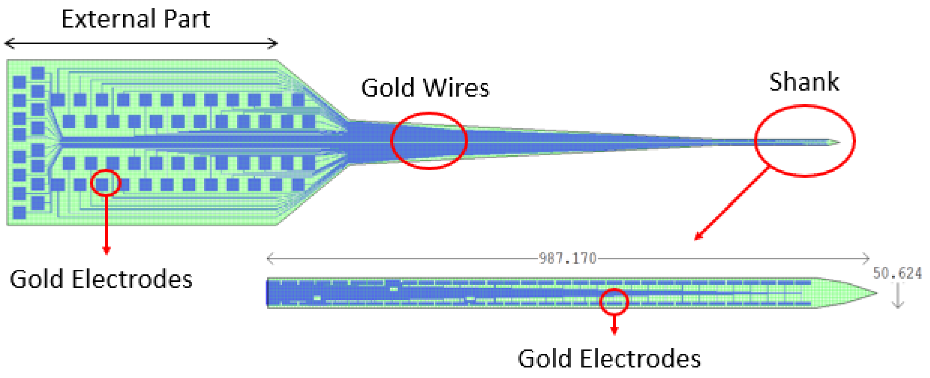

Figure 2.2: Top view of the probe with electrodes.

confined space.

As shown in fig. 2.2 the probe can be divided functionally in two main parts: the external part and the shank. The external part, the one that will remain outside of the tissue, has the function to interface a Printed Circuit Board (PCB) and an Optical Fiber in order to provide respectively an electrical and an optical source connections to the main components of the device. Its dimensions are $2200\mu m$ in length, $1300\mu m$ in width and around $530\mu m$ in thickness, chosen to ensure a good handling of the device, to contain 64 gold electrodes to be connected with an external PCB and the a central groove for a correct positioning of the couple optical fiber.

The shank is the most important and delicate part of the probe since it has the active role of the device: to be inserted in the cerebral tissue and to perform the device's functions. That's why it has been designed in order to ensure a good mechanical stability, to not be broken when inserted, and optimized geometry to minimize the brain damage. Starting from the end of the external part the probe is tapered in width from $1300\mu m$ to the final 50μ of the active part, that presents $25\mu m$ in thickness and around $1mm$ in length. Furthermore the end of the shank is tapered again in order to ensure a sharp tip for the penetration of the tissue. The active part is composed of: 64 gold electrodes for the sensing of neurons' action potential; ring resonators and focusing gratings respectively for the selection and the illumination of the different light spots that stimulate certain zone of the tissue.

In the following a detailed description of the electrical and the optical layer is carried out.

2.1.1 Optical Circuit

The main component of the optical layer, as discussed before, are waveguides, ring resonators and focusing gratings. They are made by a Si_3N_4 core and SiO_2 cladding in order to propagate visible light in the blue range, at $450nm$, that is the the wavelength needed to activate the transmembrane ion channels, expressed trough the genetically modification of neural cells, Channelrhodopsin-2 (CHR2) [34], ensuring low absorption losses. The choice of Si_3N_4 as core is driven by its optimal optical properties for this working range: thanks to is high refractive index of around 2.02, respect the one of silicon dioxide (1.47 at 450nm), it allows a good confinement with low propagation losses.

The optical circuit, as shown in fig. 2.3, is mainly made of a

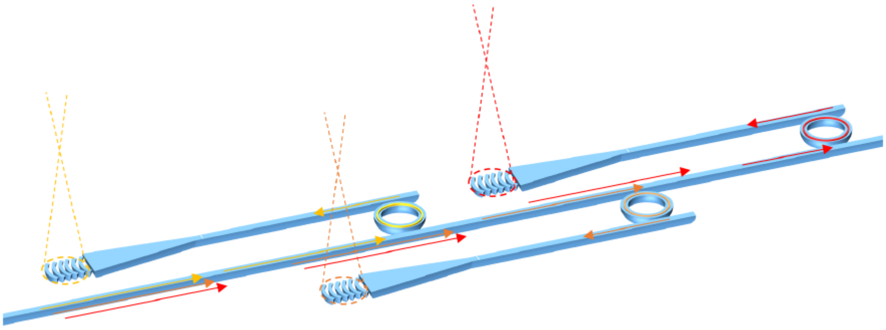

Figure 2.3: Schematic representation of the optical system.

central waveguide that starting from the groove, in the external part, runs through all the probe. When it reaches the shank, it is coupled to several ring resonators which in turns bring the light to secondary waveguides up to the respective output gratings able to to focus light in a few microns spot at a certain distance. A detailed view is shown in fig. 2.4. Thanks to this design choice, switching the input wavelength one is able to light selectively different spots, corresponding roughly to different cortical layer. The light sorting system between the different output is based on a resonance effect happening in the rings. The whole optical system have been devoloped through simulation done using the software Lumerical®, that implements a Finite-difference time-domain (FDTD) solver. [33]

In the following particular description of each component and the physical working principle of the whole optical system will be given.

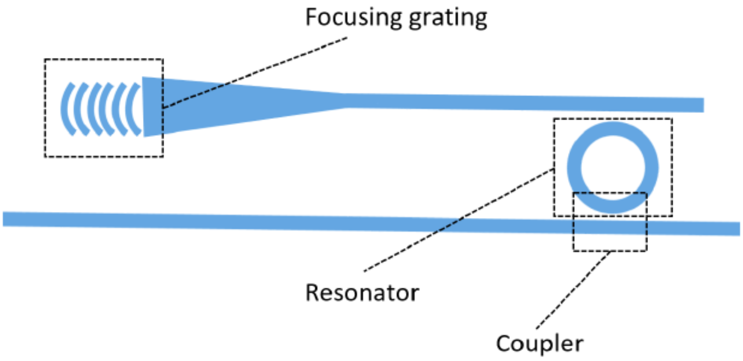

Figure 2.4: Detail of the a secondary waveguide, and its output grating, coupled through a ring resonator.

The Waveguides are designed to run through all the probe: form the external part, where the main waveguide is coupled with an optical fiber in the groove, to the shank where several secondary waveguides are present. Each waveguide is $160nm$ thick in order to obtain a single mode propagation of the light, and $4\mu m$ in width in the largest part, to ensure an easier coupling to the optical fiber (around $4\mu m$ core), up to $300nm$ wide in the smaller part. The way the light is directed between the different optical paths is based on a coupling effect that occurs when the waveguides are placed in proximity with each other. The physical mechanism can be explained considering this coupling effect for two straight waveguides. Considering two identical parallel waveguides separated by a gap, as in fig. 2.5, solving Maxwell field equations one is able to find the propagation modes. Assuming two identical waveguides, both single mode and weakly coupled, if the gap is small enough the mode in one waveguide can propagate on the other one next to. Solving the following

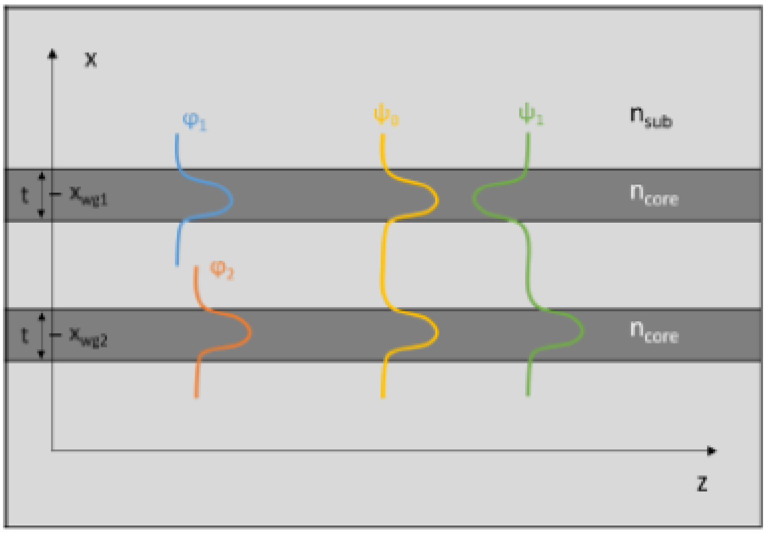

Figure 2.5: 1D coupler schematic representation.

wave equations for each waveguide, the solution turns out to be a linear combination of the modes of each waveguide:

$$\Delta\phi_1 + (k_0^2 n_1(x)^2 - \beta^2)\phi_1 = 0 \tag{2.1}$$

$$\Delta\phi_2 + (k_0^2 n_2(x)^2 - \beta^2)\phi_2 = 0 \tag{2.2}$$

where referring to fig. 2.5, β is the propagation constant of the mode and $n(x)$ in the transversal non-homogeneous refractive index. Performing further mathematical calculation, the following system can be obtained:

$$\begin{cases} a_i(n_{eff}^2 - N_{eff}^2) + b_i k = 0 \\ a_i k + b_i(n_{eff}^2 - N_{eff}^2) = 0 \end{cases} \tag{2.3}$$

where n_{eff} is the effective refractive index of the modes; k is the coupling coefficient; N_{eff} is the ratio between the propagation constant β of the mode and the coupling coefficient k; a and b are constants. Due to the identical waveguides assumption , k

appears in both equations. For homogeneous systems the non-trivial solutions are given when the determinant is equal to zero. So

$$N_{eff}^2 = n_{eff}^2 \pm k \tag{2.4}$$

finally adding the normalization conditions the two fundamental modes of the system can be found:

$$\Psi_0 = \frac{1}{\sqrt{2}}(\phi_1 + \phi_2)e^{-jk_0\sqrt{n_{eff}^2+kz}} \tag{2.5}$$

$$\Psi_1 = \frac{1}{\sqrt{2}}(\phi_1 - \phi_2)e^{-jk_0\sqrt{n_{eff}^2-kz}} \tag{2.6}$$

where ϕ_1 and ϕ_2 are the fundamental modes, as shown in fig. 2.5. From this results it can be seen that the coupling coefficient k affects directly the propagation constant of the mode Ψ_1 and also regulate the power transmitted to the second waveguide. If k is small Ψ_0 and Ψ_1 have similar wavelength and velocity and their superposition gives back the mode ϕ_1, this means that the mode can be fully transmitted in the second waveguide after long distances, while an high k allows to the transmit the full power in short distances.

In our case the coupling happens between a waveguide and a ring, and not between two straight waveguides, although this the coupling coefficient k keeps the same qualitative role. Therefore it is important to analyze this parameter to consider it in our different case:

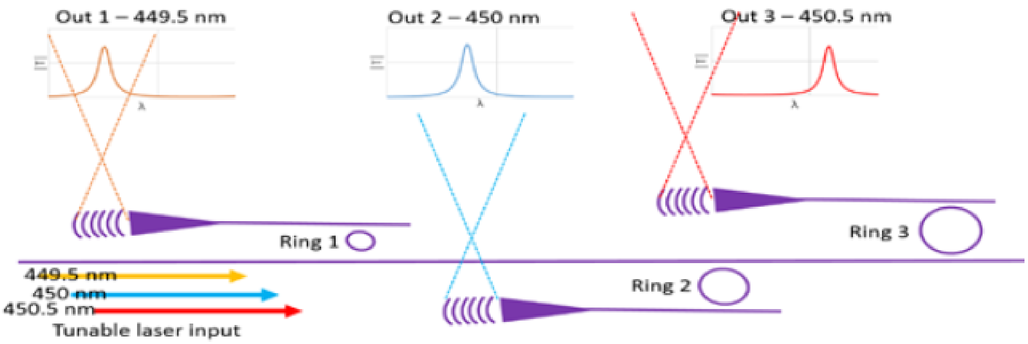

Figure 2.6: Sorting system mechanism: each ring resonator, of different diameter, enters in resonance for different wavelength. Then through the grating the light is focused at a certain height h.

$$k = \int \int_A \phi_2(\Delta(n_2^2))\phi_1^* dS \tag{2.7}$$

where n_2 is the refractive index of the second waveguide. Equation 2.7 shows that k comes from the overlap of the two wavefunctions. It mainly depends on the gap between them: a small gap ensures an higher overlap and so an higher coupling.

The Ring resonators are the optical elements that allow to light sorting mechanism between the several secondary coupled waveguides, that at the end will drive the light until the focusing grating. The rings coupled to the principal waveguides, according to the principle discussed before, act as resonators. The sorting mechanism depends on the wavelength, as shown in fig. 2.6: depending on the ring's diameter, for certain wavelegnths, it goes in a resonance state ad it is able to select a specific frequency in order to activate or not a specific output grating. Generally a

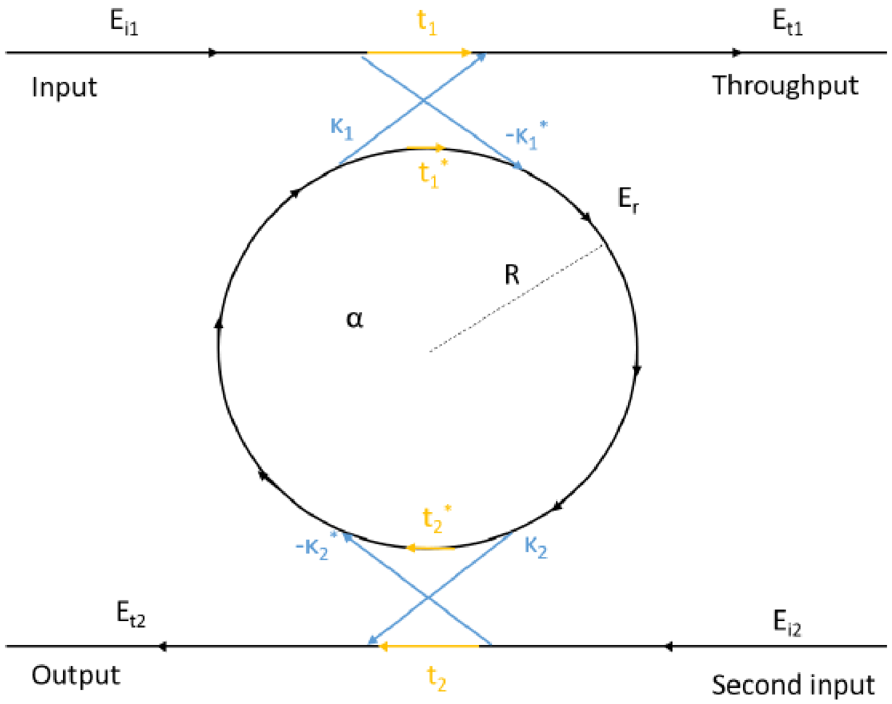

Figure 2.7: Ring resonator working principle.

ring resonator is a simple structure working as a filter for specific frequency.

The coupling between the waveguide and the ring can occur for a large range of frequencies due to its circular shape, but although the big coupling range the establishment of a stationary wave in the resonator can happen only if the incoming wavelength is a submultiple of the ring's circumference: only in this case the wave can constructively interfere with itself. This principle is shown in fig. 2.7.

Considering two waveguides and a resonator in between them, and assuming a unidirectional, lossless coupling and a conservation of the polarization during the power transfer, the transmitted power P_{t2} can be defined as:

$$P_{t2} = \frac{(1 - |t_1|^2)(1 - |t_2|^2)\alpha}{1 - \alpha\, |t_1|^2\, |t_2|^2} \tag{2.8}$$

where α takes into account the power lost in the ring, mainly fue to curvature losses, t_1 and t_2 are the transmittance coefficients of the two waveguides. The transmitted power P_{t2} tends to one if $t_1 = t_2$ and $\alpha = 1$. In real systems it is practically impossible to achieve $\alpha = 1$, close values can be obtained for large curvature of the ring, moreover experimental losses may be due imperfection or anisotropies coming from the fabrication process and cannot be taken into account during the simulation phase.

An important figure of merit describing the ring resonator is the Free Spectral Range (FSR), that is the difference between the wavelengths corresponding to two resonant conditions:

$$FSR = \Delta\lambda = -\frac{2\pi}{2\pi R}\left(\frac{\partial\beta}{\partial\lambda}\right)^{-1} \tag{2.9}$$

if difference in waveleghnts $\Delta\lambda$ is small enough so that the variation of β with respect to λ can be neglected, the expression can be simplified as

$$FSR \simeq -\frac{2\pi}{2\pi R}\left(\frac{\beta}{\lambda}\right)^{-1} = \frac{\lambda^2}{n_{eff} 2\pi R} \tag{2.10}$$

where R is the radius of the ring.

Another important figure of merit is the Full Width at Half Maximum power (FWHM), that is the width of the peak at $-3dB$ respect its maximum:

$$FWHM = \frac{\lambda^2}{\pi(2\pi R)n_{eff}}\frac{t}{1-t^2} \tag{2.11}$$

where the transmittance coefficients are equal and real $t_1 = t_2 = t \in \mathbb{R}$, this holds for a symmetric system.

This quantity can allow to extract the Q factor of the system: it measure the quality of a resonator and its ability in store energy.

$$Q = \frac{\lambda}{FWHM} = \frac{\pi(2\pi R)n_{eff}}{\lambda}\frac{1-t^2}{t} \tag{2.12}$$

The Optical Focusing Grating is the last element that the light meets before it reaches the neural tissue. Once the incoming waves have been selected by the ring resonators they arrive to this peculiar element that works both as lens and diffraction grating. In general a diffraction grating can be considered as a collection of diffraction elements, for example a periodic pattern of reflecting grooves on a substrate, each separated by a distance comparable to the wavelength of the light used. The fundamental physical effect exploited in a diffraction grating is the spatial modulation of the refractive index: when an electromagnetic wave is forced on a grating its electric field amplitude and/or phase will be modified due to the periodic variation in refractive index in the region near the surface of the grating. [35] Diffraction gratings commonly work in reflection or transmission, where the input light comes from an external optical fiber placed over the grating. As shown in fig. 2.8, in general considering a light ray of wavelength λ

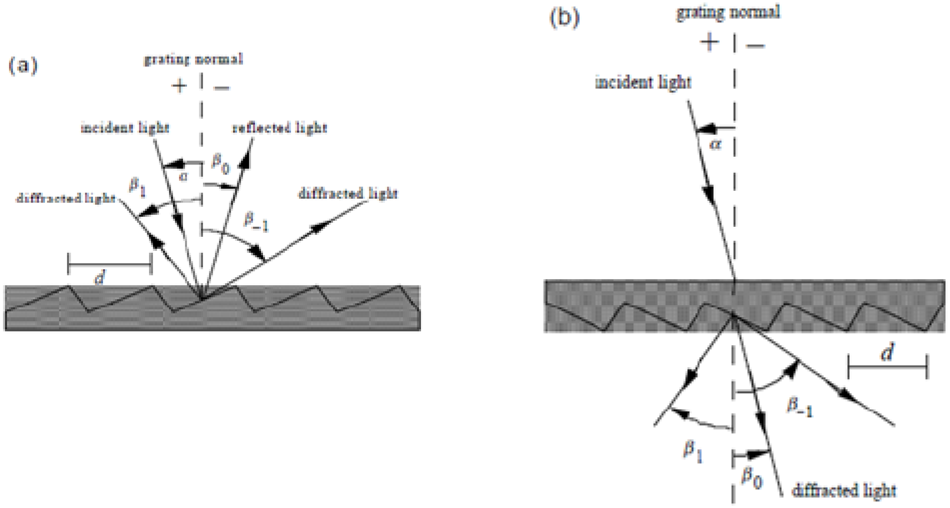

Figure 2.8: General diffraction grating scheme.

impinging the grating, with a groove spacing d called pitch, at an angle α, it is diffracted by along a set of angles β_m, with m being the diffraction order. [35]

Because of the purpose of the neural probe, here instead it has been designed a device able to output light, coming from the waveguide, and focus it at a certain distance ($\simeq 20\mu m$ for $450nm$ [33]). This choice is driven from the physiological consequence of the probe inserted in the tissue. As discussed before, a foreign body inserted in the tissue causes several damages killing the neurons in contact with it and creating a layer of non active cells. Focusing the light several microns over the neural interface allows to overcome this layer. The focusing gratings consist in chirped and curved grooves able to deflect light rays at different angle, the light ray intersection is the focal point. Therefore, the beam shape is the one of a cone, as shown in fig. 2.9. These characteris-

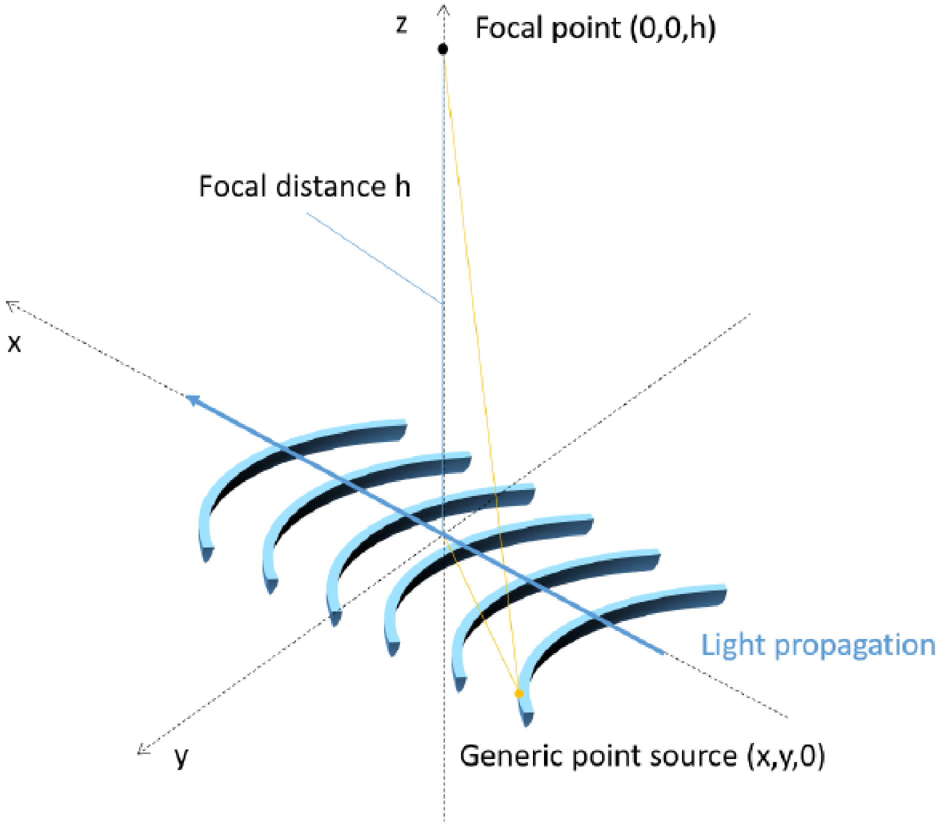

Figure 2.9: Focusing grating working principle.

tics allow to control the power delivery and the spatial resolution: as the cone shrinks up to the focal point the power density increases up to its maximum, where it is enough to activate the light-activated transmembrane channel exploited, $CHR2$. The aim of using these kind of illumination system is not to illuminate a single neuron but a subpopulation of neurons placed above the probe, in order to make them fire an electrical signal and try to catch it, with the goal to estimate how the neurons networks work.

The developed gratings are $4\mu m$ wide, in order to prevent interferences with the sidewalls, and $10\mu m$ long, depending on the number of grooves. The latter have a thickness of $160nm$, as the whole Si_3N_4 layer exploited for the optical system, where each point can be considered as a light point source. The space and the chirped spacing between the grooves have been selected so that light coming from each point interferes constructively in the focal point. From an analytical point of view, the interference condition is:

$$\frac{2\pi n_{eff}}{\lambda_0}x + \frac{2\pi n_m}{\lambda_0}\sqrt{x^2 + y^2 + h^2} = m2\pi \tag{2.13}$$

Then it must hold:

$$\frac{n_{eff}}{\lambda_0}x + \sqrt{x^2 + y^2 + h^2} = m\frac{\lambda}{n_m} \tag{2.14}$$

where h is the focal distance, n_{eff} is the effective refractive index of the mode propagating in the grating and n_m is the refractive index of the medium above the grating plane with $m \in \mathbb{N}$. [36]

2.1.2 Electrical Circuit.

The top layer of the device consists in an electrical circuit, obtained through a lift-off process, made of evaporated Gold over a thin Titanium adhesion layer, that will be discussed better in the fabrication steps. The goal is to exploit a set of gold electrodes in the shank for the detection of neural electrical signals. These golds electrodes are connected through wires to the topmost part of the probe, where another sets of gold pads is present, in or-

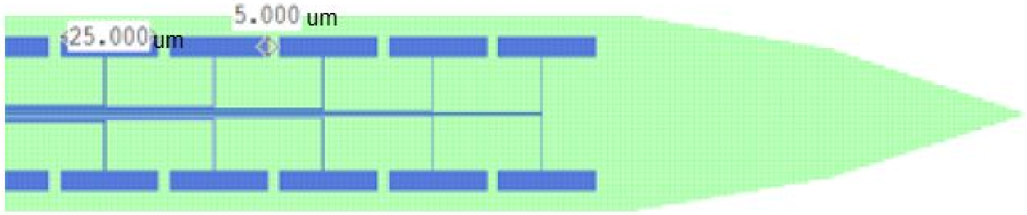

Figure 2.10: Electrodes in the shank for neural recording.

der to interface the circuit with an external PCB, linked through wirebonding. The choice of gold as material for the electrical neural interface is due to its particularly good low resistivity and biocompatibility.

The Electrodes in the shank shown in fig. 2.10, have a rectungalar shape with dimensions of $25\mu m \times 5\mu m$: $25\mu m$ because it is the average dimension of cortical neurons both in human and rodents [37]; $5\mu m$ chosen to ensure for enough space for the positioning of the wires and to not increase the width of the shank in order to prevent brain damage. The total number of electrodes is 64, divided in two columns for each side of the shank. Moreover they are spaced of $3\mu m$ from each other and $5\mu m$ from the edge. The dummy space left from the edge accounts for fabrication tolerances and possible misalignments.

These 64 electrodes are then linked with 64 pads placed in the upper part of the probe through gold wires of $120nm$ in width, $450nm$ pitch, in the shank.

The Electrodes in the external part instead have a square shape with dimensions of $100\mu m \times 100\mu m$ thanks to the higher space available and to ensure a good connection for the wirebonding to the external PCB.

2.2 Processes background

In the following, an overview of the main processes exploited in the fabrication of the neural probe will be given. Lithography, etching, and deposition techniques will be discussed together with the respective tools used at Nanofabrication facility of the Molecular Foundry.

Starting from the most used techniques, Optical and Electron Beam Lithography have been widely exploited. The lithographic processes comprise three main steps: Exposure of the resist (photoresist or e-beam resist); Development of the resist; Pattern transfer.

2.2.1 *Electron Beam Lithography*

Electron beam lithography is one of the most common techniques for patterning at the nanoscale, it is based on the definition of submicrometer features by the scanning of a focused energetic beam of electron on a resist. The energetic absorption in specific areas causes intramolecular phenomena that define the features in the polymeric sensitive resist. The latter, when exposed to the electron beam, is physically or chemically, modified due to the energy released by the e-beam. Then, this mechanism creates a latent image that is materialized during the chemical development. The parameters that influence the final design on the resist are the shape and characteristics of the electron beam, the energy and intensity of electrons, the molecular structure and thickness of the resist, the electron-solid interactions, the chemistry of the development, its condition (time, temperature...), the irradiation process from the design structure to the beam deflection and control. There have been lot of advantages in the beam characteristics from the development of stable and cold emission filaments to the decrease of the effective beam diameter until few nanometers. However, the main limitation in the resolution is not in the electronic radiation but in the resist chemistry. It introduces certain requirements in terms of dose and pre post exposure processing that are necessary for adequate results. [27] The tool used is a Vistec VB300 electron-beam lithography system.

2.2.2 *Optical Beam Lithography*

Optical lithography is a photon-based technique consisting in the projection of an image into a photosensitive emulsion (photoresist) spun onto the substrate. This technique has been developed offering different implementations, both in wavelength and optical configurations: wavelength range from the visible to the deep Ultraviolet; while the optical configurations vary from the direct shadow casting to the multi-element refractive and/or reflecting imaging system. However, differently from the E-beam lithography the wavelength is the main limitation factor in the resolution of optical lithography systems together with the concept of diffraction. Also the illumination source coherence plays an important role in the resolution limit: modern exposure systems are able to employ extremely narrowband sources allowing to neglect the effects of temporal coherence and leaving only the spatial coherence resolution limitations. [28]

2.2.3 Etching

Etching is the key process for removing material from surfaces in order to achieve the pattern transfer from the developed resist to the substrate. There are two types of etching: wet and dry etching. In dry etching the material is removed exploiting a plasma, in wet etching instead the material is removed by a chemical solution that attacks it.

Wet Etching

Also known as chemical etching, it is a material removal process that uses liquid chemicals to remove materials from the substrate. It can be divided into two categories:

- **Anisotropic wet etching**: in this case the liquid etchants attack a crystalline materials at different etching rates depending on the crystalline orientation of the surface exposed. The difference in etching rates can be very large.

- **Isotropic wet etching**: here instead the material is removed in all the direction at similar speed. Generally the wet etching is always isotropic. [29]

Dry Etching

Also know as plasma etching, it is the only commercial technology for anisotropic removal of the material from the surface. The material removal is obtained through the plasma exploiting high kinetic energy of particles, chemical reactions or a combination of both. [30]

- **Physical dry etching**: it requires high kinetic energy (Ions, electrons or photons) inside a plasma to remove the substrate atoms. The high energy particles knock out the atoms from the surface, the material evaporates after have left the substrate. Given the fact that there is no chemical reaction taking place, only the material which is unmasked will be removed.
- **Chemical dry etching**: it involves chemical reaction between the etchant gases and the surface enhanced by the plasma. It is usually isotropic and exhibits high selectivity. However, anisotropic dry etching has the ability to etch with higher resolution and higher aspect ratio than the isotropic one, and because of the lack of directionality in the latter undercutting can not be avoided. [30]

- **Reactive Ion Etching**: This is one of the most widely used process in industry and research which uses both physical and chemical mechanism to achieve high level of resolution, making the process mush faster. The high energy collision from the ionization in the plasma helps to dissociate the etchant molecules into more reactive species. That is, cations are produced from reactive gases which are accelerated with high energy to the substrate and chemically react with it. [30] The tool exploited in RIE process is an Oxford Plasmalab 80.

2.2.4 Plasma Enhanced Chemical Vapor Deposition (PECVD)

Plasma Enhanced Chemical Vapor Deposition is one of the most important plasma-assisted deposition technique for producing films on surfaces. Usually device structures are sensitive to temperature causing standard high-temperature deposition processes to be not used in a device process flow. However, thanks to the nonequilibrium nature of low-pressure processing discharges, films can be deposited at lower temperatures. Moreover, films can be deposited with improved properties as nonequilibrium chemical compositions and crystal morphologies that are not reachable under equilibrium deposition conditions at any temperature. Standard Chemical vapor Deposition consists on a thermally activated set of gas-phase and surface reactions that produce a solid product at the surface. In PECVD instead the gas-phase precursors and often the surface reactions are controlled or strongly modified by the plasma properties. [31]

2.3 Atomic Layer Deposition (ALD)

Atomic Layer Deposition is a chemical gas phase thin film deposition technique based on the alternation of saturative surface reactions: with respect to other chemical vapor deposition methods, the source vapors are pulsed into the reactor alternately separated by purging or evacuation periods. Each precursor exposure step saturates the surface with a monomolecular layer, resulting in an unique self-limiting growth mechanism with several advantageous properties: excellent conformity and uniformity, simple and accurate film thickness control based on the number of cycles performed. The ALD film growth takes place in a cyclic manner, where each one consists of the following steps:

1. Exposure of the first precursor;
2. Purge or evacuation of the reaction chamber;
3. Exposure of the second precursor;
4. Purge or evacuation.

Depending on the process, one cycle can deposit from 0.1 to $3\mathring{A}$ film thickness, repeating this cycle as many time as necessary the final thickness desired can be achieved. The reactions which takes place each exposure step depend largely on the presence or the absence or reactive functional groups on the surface of the growing film. Then, as a result the ALD provides perfect conformity and trench-fill capability as well as good large area uniformity and large-batch capability and good reproducibility. [32] The tool exploited fro ALD technique is an Oxford FlexAl, Plasma-Enhanced ALD.

CHAPTER 3

Fabrication Steps and Results

In the following a step-by-step description of the fabrication process, together with several optimization results performed in this thesis work, will be given.

The entire fabrication process of the neural probes is based on a commercial 4″ wafer, Lionix® Triplex Wafer, layered with a central $525\mu m$ substrate of Si, then $2.5\mu m$ of SiO_2 and $160nm$ of Si_3N_4 deposited on both sides by Low Pressure Chemical Vapor Deposition (LPCVD) technique. The cross section is shown in fig. 3.1.

This wafer is a commercially available substrate with $< 100 >$ plane orientation, and one of the surface is polished. It ensure an high quality Si_3N_4 with very low loss over a wide wavelength range (from $405nm$ to $2350nm$), and it permits to directly pattern $Sio_2 - Si_3N_4$ waveguides on the substrate. [38]

The first step of the fabrication is the definition, by electron beam lithography, of the alignment marks necessary to correctly

Figure 3.1: Lionix® Triplex wafer cross section.

superimpose the several lithography steps that follow. The wafer is coated, on the polished side, with a positive electron beam resist (ZEP 520A [44]), then exposed by e-beam lithography and developed in Amyl Acetate. Once developed, an deposition through electron beam evaporation of Gold, over a thin $10nm$ Ti layer in order to guarantee a good adhesion, is performed. Finally well defined alignment marks are obtained performing a liftoff process in PG Remover [45] at 80° C.

3.1 Fabrication Optical circuit

The second step consists on the fabrication of the optical system with all its components as the waveguides, the rings resonator and the gratings. The process in shown in fig. 3.2.

Electron beam lithography has been exploited, the e-beam resist ZEP 520A is spun over the nitride layer (ZEP 520A at 50%, at 1000 RPM, in hot plate for 5 min at 180° C, $230nm$ total thick-

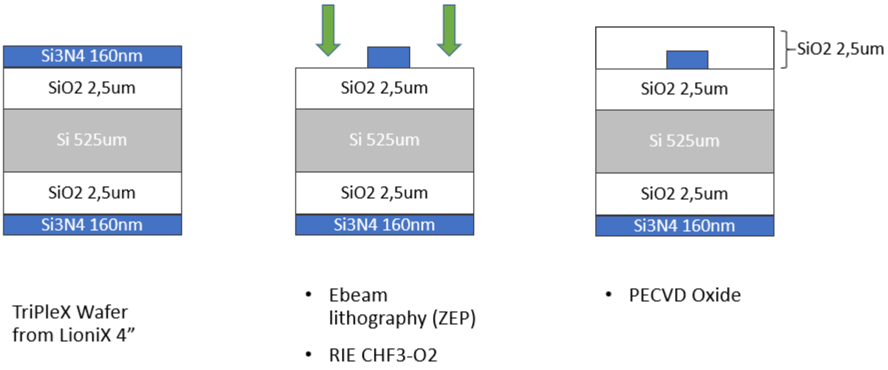

Figure 3.2: Fabrication steps to define the optical system.

ness), exposed and then developed with Amyl Acetate, as before. Then a descum step is performed to remove eventual residuals of the resist in the tranches in order to ensure a correct pattern transfer on the nitride, consisting in an oxygen plasma with a Reactive Ion Etching (RIE) tool (100 sccm O_2, $30mTorr$, $40W$ RF power, for $15s$, DC bias $\simeq 227V$). The Si_3N_4 is etched, in the same chamber, in a two step process with $CHF_3/0_2$ $(48 : 2sccm)$ chemistry: the first for $7min$ $30s$, $55mTorr$, RF power $49W$, DC bias $\simeq 214V$; the second with same parameter but an higher RF power of $97W$, DC bias $\simeq 214V$ and lower etching time $1min$ $30s$. The choice of a two step process with an increasing power is taken in order to open correctly the coupling gap between the waveguides and the rings. This feature is particularly challenging because of its extremely small dimension ($30nm$), therefore it has to be as much precise as possible to achieve a correct coupling. The trench depth depends on its width, because diffusion of gaseous chemical species at its bottom is limited in narrow trenches preventing the arrival of gases at the their bottom. The extremely thin dimension of the feature leads to a shallow etching and a non-completely opened gap. Therefore the first step at lower RF power ensures a chemical etching that removes the most of the material and then the second step at higher RF power, where the etching is more physical and anisotropic, ensure a complete opening of the gap.

Once transferred the optical pattern, the remaining resist is removed with a sonication in dichloromethane and then acetone, and $2.5\mu m$ of SiO_2 is deposited through Plasma Enhanced Chemical Vapour Deposition (PECVD). This oxide layer have been optimized to minimize the optical losses, for this purpose the fabrication process has been followed by optical power measurements.

3.1.1 Results: RIE Optimization

Although the use of a high quality wafer, in which the nitride layer present propagation losses as low as $5 \times 10^{-4} dB/cm$, and waveguides losses as low as $0.001 dB/cm$ have been measured [38, 39, 40], the optical power measurements performed in fabricated waveguides showed a different scenario. Aligning a blue laser ($450nm$) through a micro-manipulator and maximizing the output, optical measurement have been recorded with the help of an optical microscope, then relating the output power of the gratings to the coupled laser output power, losses have been derived. However laser-waveguide coupling losses are non negligible. In order to determine the scattering losses a waveguide split in two with different path length have been exploited comparing their cross section output. This comparison allows to neglect the coupling losses. The measurement of cross section output power have been used because also gratings have losses, in this way the scattering losses of the waveguides have been completely decoupled from the coupling and the gratings ones. The resulting scattering losses measured, after the deposition of the PECVD top cladding oxide, were around $3-10dB/cm$. In order to reduce the losses some tests on the fabrication of the waveguide have been performed about the top cladding oxide quality and the optical system fabrication. In particular the recipe optimization used for the pattern transfer of the optical system through RIE have been studied. It have been shown that the surface roughness, rather than absorption from the bulk material, plays a major role in the loss limitation of Si_3N_4 waveguide. [40] Moreover, the major contribute to the waveguide sidewalls scattering is due to the *in situ* polymer formation typical in the dry etching processes. The polymer formed during the transfer pattern process, while it allows sidewall passivation in order to achieve anisotropic etching and vertical structures desirable for the fabrication of rectangular waveguides, often leaves residue on the sidewalls, which introduces sidewall roughness. [41] The $CHF_3/0_2$ chemistry exploited plays in two ways in the etching process according to their

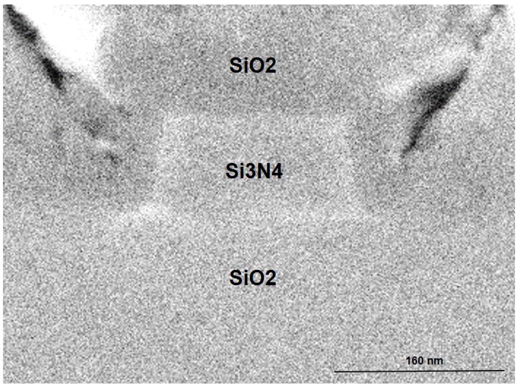

Figure 3.3: $CHF_3/0_2$ $48/2sccm$ ratio recipe, SEM cross section after cladding. The oblique cracks in top right and left come from the deposition of PECVD oxide that, nucleating on the horizontal surfaces, lead to a misalignment of the forming material planes.

ratio: an higher flow of CHF_3 allows a chemical etching of the nitride and formation of passivation sidewalls polymers, instead an higher flux of O_2, being accelerated toward the sample, gives a physical and highly anisotropic (vertical) etching and reduces the polymerization process.

Moreover, in figure 3.3, an SEM cross section of a waveguide after the top cladding deposition, is noticeable that the sidewalls are shallow. This can be explained by the fact that the recipe exploited has an high CHF_3/O_2 ratio ($48 : 2sccm$) and consequently an high polymers formation. The high concentration of polymers forms an *overpassivation* of the sidewalls that shields the horizontal surfaces surrounding the nitride, preventing the removal of material and finally giving a trapezoidal shape to the waveguides. A typical solution for the polymer formation problem is to increase the Oxygen flow, since it reacts with this residues to form carbon monoxide (CO) and carbon dioxide (CO_2) [41]

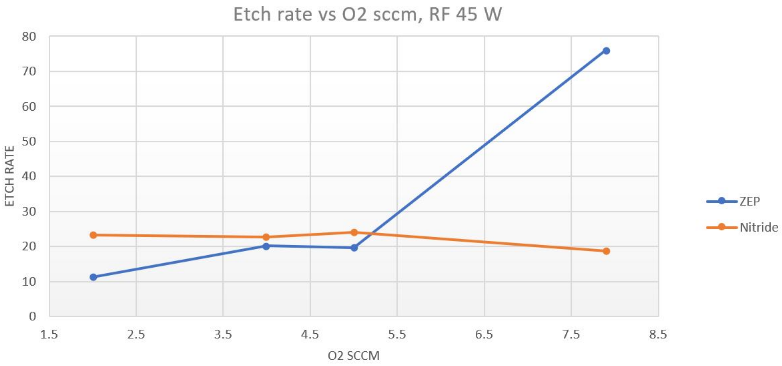

Figure 3.4: Etch rate trend of resist ZEP520A and Si_3N_4 under $CHF_3/0_2$ chemistry at constant flux $50sccm$, RF $45W$, $55mTorr$. The ZEP removal rate increases fast augmenting the relative concentration of Oxygen in the chamber. The Nitride etch rate remains almost constant.

that being volatile are then expelled from the reaction chamber. In order to achieve rectangular waveguides and reduce the surface scattering, a solution appeared to be to increase the O_2 flux. However, an higher flux of Oxygen may also reduce the resist used as mask and completely prevent the polymer formation leading to unwanted undercuts. Therefore, several trials gradually decreasing the $CHF_3/0_2$, flux ratio have been performed, with constant total flux of $50sccm$, constant pressure ($55mTorr$) and RF power ($50W$). The tests have been carried without changing the exposure step: with the same dose and resist thickness (ZEP 520 A $230nm$).

In order to prevent an high removal of resist, the removal rate of the ZEP at higher flux of Oxygen have been calculated together with the one of the nitride. From these preliminary tests came out that the ZEP removal rate increases faster than the nitride one,

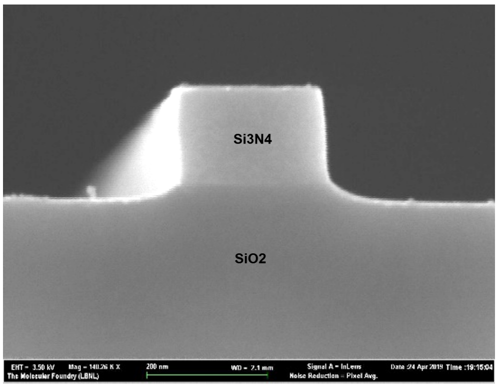

Figure 3.5: Lower CHF_3/O_2 45/5$sccm$ ratio and lower pressure 30$mTorr$ recipe, SEM cross section after cladding.

shown in 3.4 , under the same total flux of 50$sccm$, then in order to completely etch the nitride for all the 160nm of thickness and do not remove the mask the working pressure have been changed accordingly. Lower reactor chamber pressure allows lower total concentrations of chemicals and consequently a lower interaction of the Oxygen with the resist, slowing down the resist removal. Moreover, having a lower pressure works in favour of the physical action of the plasma, since the Ion's mean free path increases letting them acquire higher kinetic energy. [43] Finally, in fig. 3.5 is shown an SEM cross section of a waveguide fabricated with CHF_3/O_2 ratio of 45/5$sccm$ and a pressure of 30$mTorr$, steeper sidewalls have been obtained, respect the previous recipe used in fig. 3.3.

Although a rectangular profile have been obtained, the optical measurement, performed to validate the assumptions previously done, did not show improvements. Indeed higher losses for the waveguide fabricated with the new recipe have been found. The reduced pressure and the higher flux of Oxygen could have lead to an higher top surface roughness of the waveguide, due to the higher kinetic energy of Oxygen ions bombarding the sample, increasing the scattering of the light. However, in order to find a cause further characterization (such as compositional and roughness analysis) have to be carried out. Moreover, roughness analysis would be an hard task because for thin waveguides, hundreds of nanometers, even few nm roughness can give significant losses. [42] Future works to achieve a better optimization could be the use of an hard mask or a thicker layer of resist with the relative exposure optimization.

3.2 Results: Planarization step

One of the challenges of the fabrication process was the integration of the optical and the electrical layer.

Once fabricated the optical system, over the top oxide cladding in correspondence of the waveguides, the rings and the gratings, hills were present. As a matter of fact, the optical elements are $160nm$ in thickness, therefore after the oxide deposition process this relief is projected over the top leading to a non-planar surface. The electrical layer built on top used to suffer of the non-uniformity, as shown in fig. 3.6. The critical points were the wires, because of the hills and valleys they met, several interruption along their path used to lower down the total number of working electrodes.

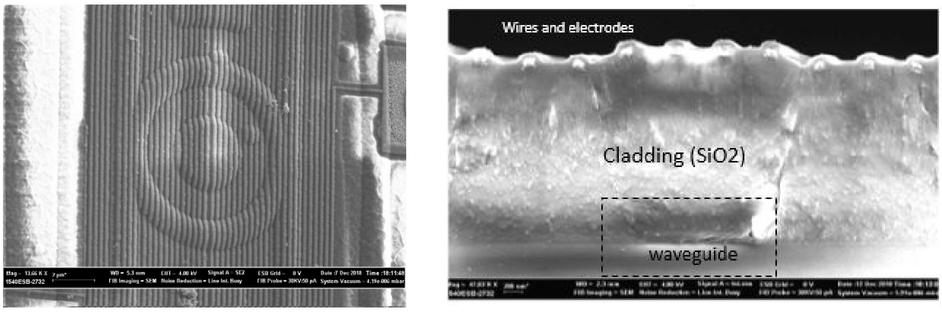

Figure 3.6: SEM top view and cross section of the shank before planarization.

The solution adopted is a planarization of the surface exploiting a flowable oxide, the Hydrogen Silsesquioxane (HSQ). This material had attracted lots of attention in the semiconductor industry thanks to its low dielectric constant, easy processability, good planarization of surfaces and excellent gap fill capability. [46] Its general chemical composition is $(HSiO_{3/2})_n$, if thermally processed the $Si{-}H$ bonds tend to dissociate and its porous structure is rearranged into a network structure. Therefore, HSQ spun over a substrate when cured with temperature tends to shrink, applying stress on the substrate, and to change its refractive index. [47, 48, 49]

After some optimizations a layer of HSQ have been obtained ($\simeq 500nm$), to not induce too much stress to the structure, with a refractive index that matches as much as possible the one of the top cladding of 1.47. The scheme is shown in fig. 3.7

Therefore this planarization layer step consists in spinning the HSQ over the wafer and then cure it. Good results have been obtained, as shown in fig. 3.8. Moreover, electrical and opti-

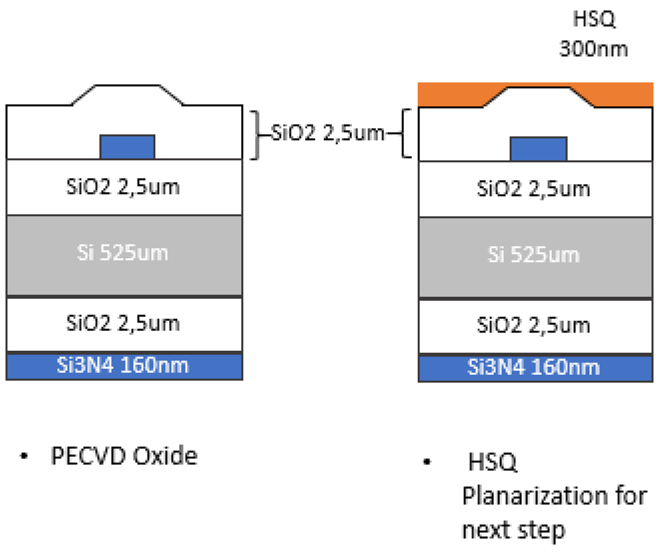

Figure 3.7: Scheme of the planaratization process.

cal measurements have been performed, respectively on the electrodes and on the optical system, in order to ensure the same performances after the planarization step with HSQ. No additional optical losses on the waveguides have been achieved, performing the same type of measurements discussed before. Furthermore, the electrical circuit fabricated in a planar substrate (Si_3N_4 on Si wafer have been used) shows the same number of working electrodes respect the one deposited on an HSQ planarized wafer. In the next section a deeper overview on the wires, electrodes and their characterization will be given.

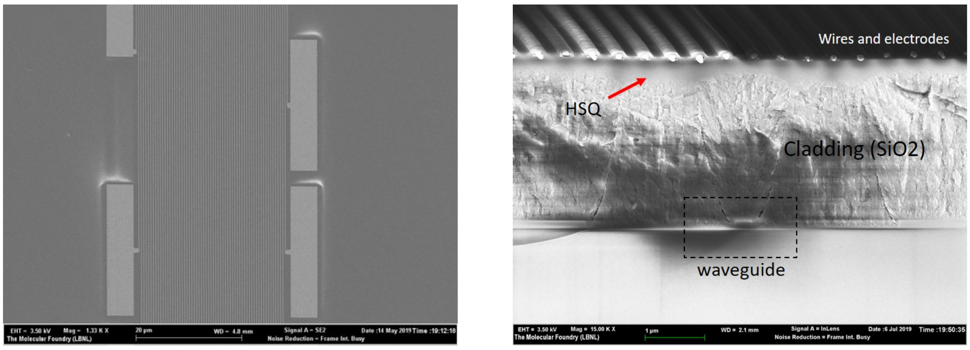

Figure 3.8: SEM top view and cross section of the shank after planarization.

3.3 Fabrication Electrical circuit

Once the wafer is planarized the next step in the fabrication of the neural probes is the integration of the electrical system, that is shown in fig. 3.9. As introduced before, the features are very small, in particular the wires, this is why electron beam lithography is again exploited with the same procedure as before: $ZEP520A$ is spun over the wafer at 4000 rpm, exposed through e-beam lithography at $100kV$, then an high power ultrasonic development in Amyl Acetate. As already done for the alignment marks, in order to ensure a correct adhesion of the gold onto the HSQ, a $10nm$ layer of Titanium (Ti) is evaporated followed by $100nm$ of Gold (Au), by an Electron Beam Evaporator. Therefore a Lift-off process is performed in order to strip the resist exploiting hot PG remover (80° C) with stirring 80 Rpm for 1 hour. Then the wafer is rinsed in Acetone and Isopropyl alcohol to remove eventual floating Gold particles.

Figure 3.9: Summary of the electrical circuit frabrication process.

3.3.1 Results: Electrical circuit optimization

Due to the submicron features, the electrical circuit fabrication process resulted to be an extremely delicate step of the fabrication. Electrical characterization after the lift-off have been performed through a Micromanipulator® Probe Station that generates a DC voltage and record the resulting current exploiting two Tugsten microtips, as shown in fig. 3.10. This measurement have been performed mainly in order to check the working electrode yield per probe all around the wafer, and to characterize the average resistance of each electrode. Acceptable resistance values that guarantee good SNR for the neural activity recording, and in line with the expectations of the dimensions of the wires have been found to be in the order of $5 - 15k\Omega$. From several electrical characterizations came out that the working electrode yield per probe was low, around $50 - 70\%$. Open circuits in the wires were noticed in the electrical measurements by very high resistances of the order of $G\Omega$. Moreover, thanks to SEM characterizations of the samples, the presence of interruptions in the wires' path and as well short-circuit was evident, as shown in fig. 3.11, in the shank where the wires reach their lower dimension and higher density, with around $15 - 30\%$ of shorted circuited wires. Shorts circuit have been as well found in the electrical characterization steps checking the values of resistances between the electrode under test and its neighbours. In order to solve the shorts and open circuit problem several attempts have been carried out. The critical point in the fabrication steps have been found to be the dose-sonication relation, the wires layout and the lift-off process,.

The lift-off process used so far exploited the solvent Remover PG at 80° C with $60 Rpm$ of stirring for $2hrs$. Carrying out some tests, the critical point of the formation of open circuit during the lift-off process have been found in the use of the stirring. Test on chips and on wafers shown an increase of the working electrode yield per probe to $90 - 100\%$ on chip and on wafer, although the shorts remained constant. Therefore, the use of stirring, although it helps in reducing the redeposition of gold particle in the substrate, in our case the agitation leads to the rupture of the wires.

Sonication refers to Ultrasonic-assisted development. The resist sensitivity and contrast are dependent on the resist material property and on the resist process condition, such as beam energy, exposure dose and development. In order to enable very high

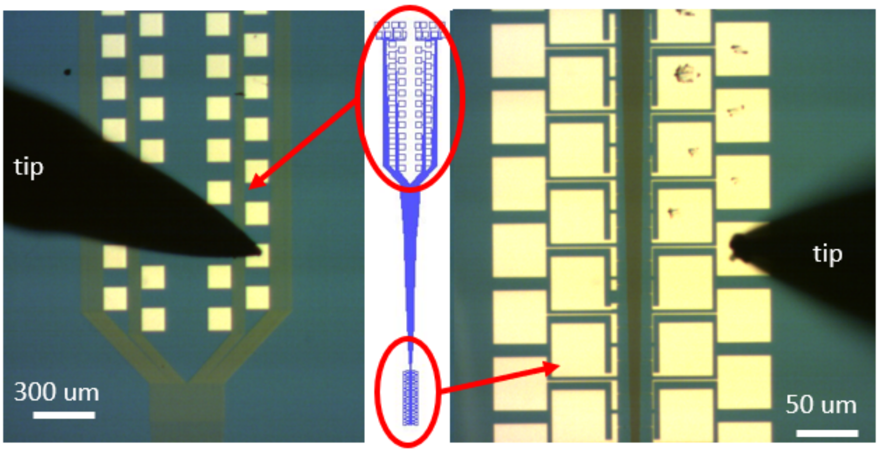

Figure 3.10: Example of electrode working test. Notice that the electrodes in the shank have been fabricated larger than the standard designed ($45\mu m \times 45\mu m$) in order to facilitate the electrical characterization.

resolution of e-beam lithography, methods as ultrasonic-assisted development have been studied. The ultrasonic agitation during the development can provide additional energy in order to dissolve exposed resist molecule trapped in the solid resist edges due to intermolecular forces, that is equivalent to exploit more electron interactions to release the trapped polymer molecules, which means higher exposure dose. Therefore the use of ultrasonic agitation can reduce the exposure dose and improve the resist contrast. [51]

The starting hypothesis was that in the shank, due to the small dimensions and pitch of the wires imposed by the maximum total width required to minimize the brain damage ($\simeq 50\mu m$), the dose used in the exposure and the sonication performed during the resist development may cause errors as a not complete removal of the resist in the wires' position causing the stripping of the gold

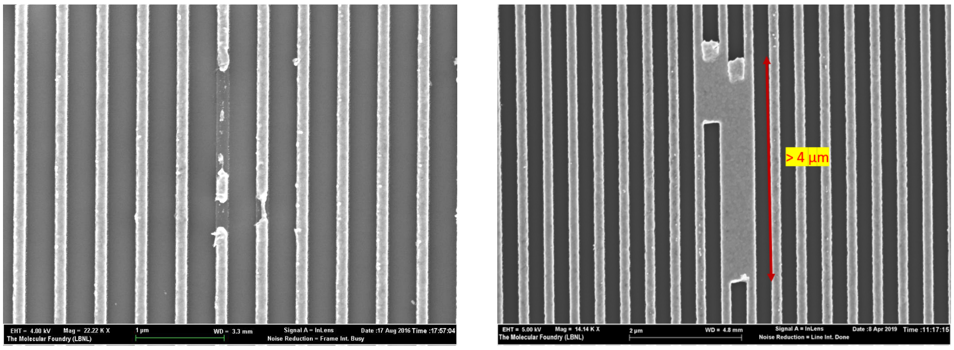

Figure 3.11: SEM characterization of the wires. On the left: presence of open circuit . On the right: presence of short circuit. Both mainly found in the shank of the probe.

and the formation of open circuit. Moreover analysing the shorts' shape at the SEM, in fig. 3.11 in the right, they are oriented along the wires up to $4\mu m$ and they look to be at the same height of the wires excluding respectively a particle contamination (that would create circular like errors) and the presence of completely unexposed resist beneath them. Therefore a cause could be the collapsing of resist lines caused to the high sonication power exploited. In order to validate these hypothesis dose-sonication tests have been performed, increasing the dose used and reducing the sonication power to not change the effective exposed region, as explained before.

From tests performed, the number of shorts circuit between the wire increased for higher doses also for lower sonication power used. Therefore, it can be explained with the fact that higher doses lead to an increase of the underexposure, increasing its aspect ratio and making easier the collapsing of the resist lines that leads to formation of short circuits. To prevent this, another

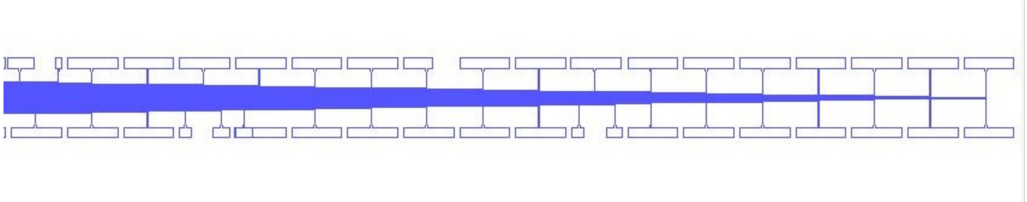

Figure 3.12: Previous electrical layout, with fixed pitch.

approach to the problem have been tried: changing the wires' layout. In the layout, as shown in fig. 3.12, the wires, coming from the external part of the probe, once reached the shank continue their path, for simplicity of the design, with a fixed pitch until the end of the probe. Going further to the end of the probe every two electrode, one per each side, the number of wires decrease. Exploiting this empty space, the pitch of the wires can be increased in order to enlarge the space between wires and reduce the probability of errors during fabrication.

With this purpose a new layout have been designed, through the software L-edit®. In the new layout the wires step away from each other, reaching the end of the shank, thanks to the space left by the external two wires that already reach the corresponding electrodes, up to fill all the space between the electrodes. In this way the probability of resist line collapsing is reduced. Moreover, the wires increase in width as well, at the point that the pitch is high enough, to reduce eventual errors in the lithography. Particulars of the new layout are shown in fig. 3.13.

The same dose-sonication tests have been performed for the new layout, best results have been obtained for high dose and no

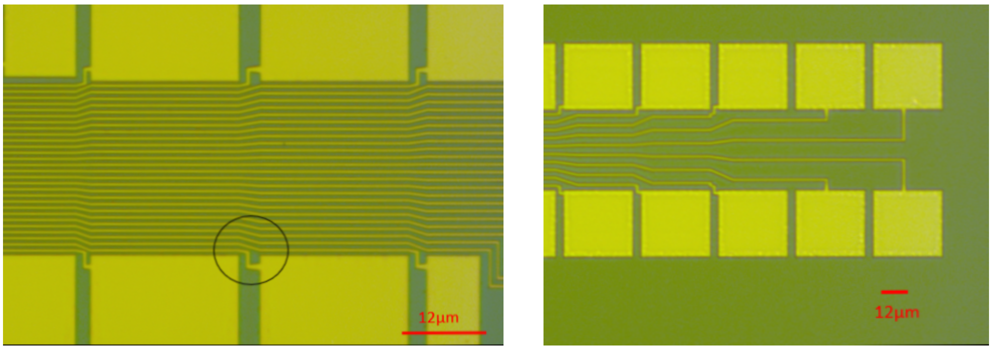

Figure 3.13: New layout with non fixed pitch. The wires step away from each other to reduce the possibility of resist line collapsing.

sonication exploited having $96.85 - 100\%$ of working electrodes and $5 - 10\%$ of short circuits between wires.

The exposure, lift-off and deposition optimization performed for the electrical layer bring some advantages on the performances of the probe. Further studies have to be carried in order to reduce to zero the number of errors along the wires, although probably for our application having a better working electrode yield than 95% is not important since sorting algorithms enable triangulation of neuron location by spatially oversampled multi-electrode recording. [21]

3.3.2 Wires passivation

The neural probe, once all the fabrication steps are completed and it is ready to be perform an in vivo test, should be able to record electrical signal only from the shank electrodes. Since the metal wires exposed to a living tissue could create shortcuts between the electrodes or as well intercept the Local Field potential deriving from the neural electrical activity, a wire's insulation is needed.

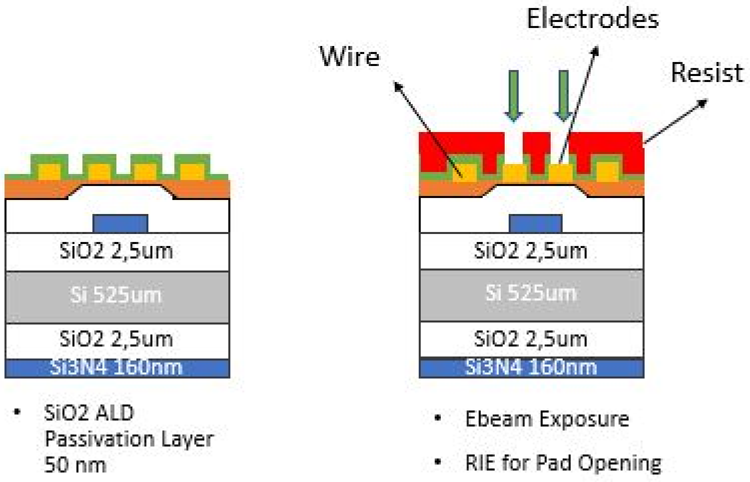

Figure 3.14: Passivation and pad opening.

Therefore, after the electrical circuit fabrication is completed, a passivation layer ($50nm$ os SiO_2) is deposited with Atomic Layer Deposition (ALD). This technique is chosen because it allows obtaining very high conformal, low stress, thin layer. After this step the whole wafer is covered by this oxide layer. In order to remove the ALD SiO_2 from the undesired parts, the electrodes, another step is performed. The wafer is aligned by the already deposited marks and then processed with an other electron beam exposure and a dry etching process. ZEP is spun and exposed in correspondence of the electrodes. Then using $35sccm$ CHF_3, $25sccm$ Ar, with RF power $100W$ and $30mTorr$ of pressure a RIE is performed to etch the exposed areas. The process is sketched in fig. 3.14. Finally the remaining resist is removed in Remover PG at 80° C.

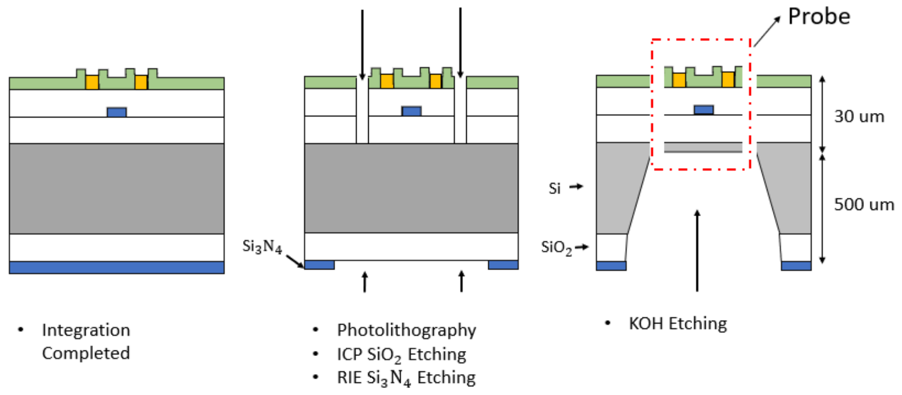

Figure 3.15: Scheme of the probe release process. Notice this cross section is in correspondence of the shank.

3.4 Probes release

At this point of the fabrication the optical and the electrical layers have been integrated at the wafer level. The next step in the fabrication process is the release of the probes from the wafer in order to achieve single devices able to be then connected to the external control system (PCB and Laser) and to be ready for an in-vivo neural experiment.

Single probes are obtained from the wafer through several steps, shown in fig. 3.15. The general idea is to define grooves on the front side of the wafer, through dry etching, to obtain the probe shape and on the back side, through wet etching in correspondence of the probe, membranes to remove most of the wafer body and release the probe, exploiting the silicon nitride layer of the Triplex® wafer as a mask.

3.4.1 Nitride mask and Front-side etching

As a first step an UV photolithography defines the Si_3N_4 mask for the backside etching: HDMS as adhesion promoter and a positive photoresist (MA-P 1215) are spun, exposed, thanks to an InfraRed alignment taking as reference the gold marks previously deposited, and then developed (with MAD 331) on the backside of the wafer. Therefore, RIE step is performed to etch the nitride defining the membranes, with CHF_3/O_2 (48/2 sccm) chemistry, RF power 100 W, for 15 min. Moreover, the front side dry etching is performed: a positive thick resist (AZ 40 XT 11d) is spun over the front side ($\simeq 40\mu m$), over HDMS, and exposed defining the probe shape and the groove for the fiber positioning; then a post exposure bake with a very slow temperature ramp is performed in order to better crosslink the polymer and to not cause cracks due to a fast bake [52]; Oxford Plasma lab 100 Viper (FY2013) is the tool used to perform the front side etching (CHF_4 35 sccm, Ar 15 sccm, O_2 15 sccm), in this way $\simeq 5\mu m$ up to the bottom cladding of the waveguides is etched, and $25\mu m$ of Si (C_4F_8 SF_6 chemistry). During the front-side etching the wafer is heated by the plasma, and since the process last long time, a poor temperature control can lead to low sidewall etching control: considerable undercut. This issue is avoided exploiting a thermal conductive polymer, the Fomblin, in between our TriPlex wafer and a $8''$ wafer used as carrier since the tool clamp support is for 8 inches wafer, that prevents the establishment of a high temperature gradient between the gas in the chamber and membrane in the nitride. Moreover the tool used exploit an He flux to keep the temperature stable at 20°. The height of the grooves are monitored using a Profilometer.

3.4.2 Back-side wet etching

As shown in the third sketch of fig. 3.15, once defined the probe in the front-side a wet etching process is performed to define the membrane under the probes. This step consist in KOH (Potassium Hydroxide) wet etching, that is one of the most used anisotropic wet etchant for cristalline silicon, for both SiO_2 and Si at 80° C with stirring, exploiting the nitride as a mask. Looking from the back-side, the nitride is $160nm$ thick, then the layers to be etched are: the oxide $2,5\mu m$ and $460\mu m$, over $525\mu m$, of 100 Si in order to leave a $\simeq 25\mu m$ of Si buffer before the grooves to prevent the KOH to go in contact the front-side, as shown in fig. 3.15. Moreover for this purpose, the wafer is clamped in a wafer holder [53], whose cross section is in fig. 3.16, that allows one side wet etching thanks to o-ring sealing. The selectivity of Si_3N_4 over the oxide and the Si 100 is respectively 3×10^{-3} and 1×10^{-5} [54], that means in order to etch $2,5\mu m$ of oxide, and $\simeq 460\mu m$ of Si the etched nitride will be $\simeq 12nm$ over $160nm$ of total thickness, meaning that the Si_3N_4 will perfectly mask for all the etching time. Because of the big difference in Etching rate of SiO_2 and Si, if micron deep scratches due to the handling

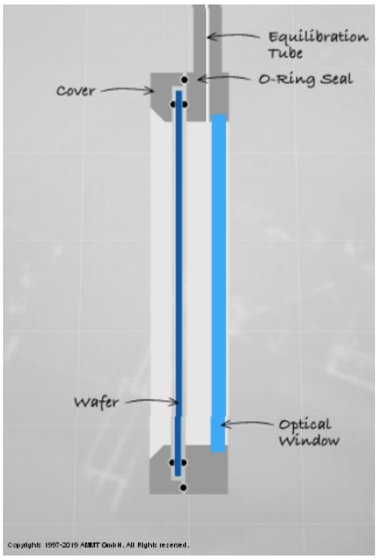

Figure 3.16: Cross section of the wafer holder exploited for the wet etching. [53]

are present in the oxide, when the Si is reached by the KOH in correspondence of them, it can result in up to hundreds of microns of Si removal in excess leading to holes in the wafer and consequently spilling of the etchant in the front-side. Therefore, however the use of the holder and the Si buffer layer, the front-side is protected with ProTeck B3, that is a front-side circuitry coating for deep backside alkaline bulk micromachining [55], in order to completely prevent the KOH spilling. The wafer holder is immersed vertically in the KOH bath at 80°C with stirring, in order to prevent the hydrogen saturation of the surface that may slow down the etching and increase the roughness. The process is monitored, after the removal of the wafer from the KOH bath and soaking in H_2O, with a Profilometer, in order to allow the correct material removal and to control the surface roughness, that at the end of the process is of the order of microns. The last step is an-

Figure 3.17: Example of a released Optoelectronic probe.

other Silicon front-side dry etching, as before, in order to remove the $25\mu m$ buffer layer. Once the release process is complete, the cross section of the shank, shown in fig. 3.17, presents from the bottom: $\simeq 25\mu m$ as Si as support layer; $\simeq 5\mu m$ of optical layer made of top and bottom oxide cladding, and nitride core waveguide; the HSQ planarization layer, $\simeq 500nm$; and on top the electrical layer made of gold circuit and ALD oxide passivation.

3.5 Packaging

In the following section an overview on the preparation of the Neural Probe for the connection to external controls is given. Once the device fabrication is completed and the probe is released in order to guarantee a better handling and to connect it with external instruments for excitation and read out, both the electrical and the optical system have to be interfaced respectively to a Printed Circuit Board (PCB), used to control the electrodes, and an Optical Fiber, to guide the light from an input laser to the probe.

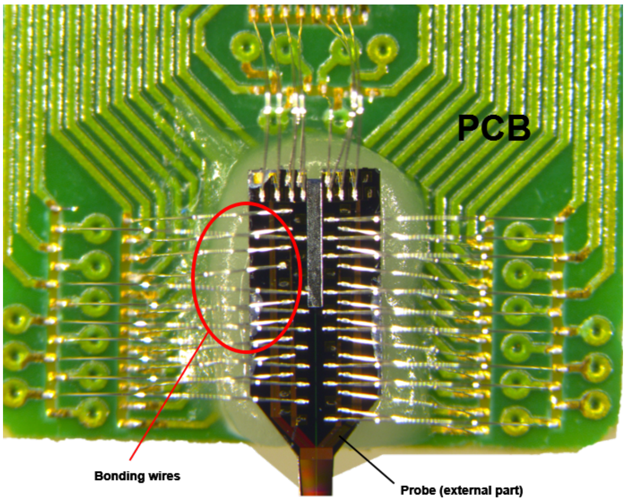

Figure 3.18: Zoom of the Probe glued and wirebonded to PCB.

3.5.1 Connection to PCB

As previously discussed, the bigger gold pads ($100\mu m \times 100\mu m$) in the external part of the probe are used as interface for the external electrical control. In order to establish the connection, the probes are glued to the Printed Circuit Board, used as support, that presents a series of pads that are then wirebonded to the electrodes on top of the probe. These pads on the PCB are then connected to *Samtec* connectors soldered on top of the PCB. Therefore, the PCB allows an easy handling of the probe and an easy access to the electrical signal by plugging the *Samtec* connectors. An example of a connected Probe is in fig. 3.18.

3.5.2 Connection to the Fiber

Once the probe is connected to the PCB, its input waveguide is ready to be coupled with an Optical fiber, aligning it and then gluing it with an UV curable glue. The U-groove designed for the

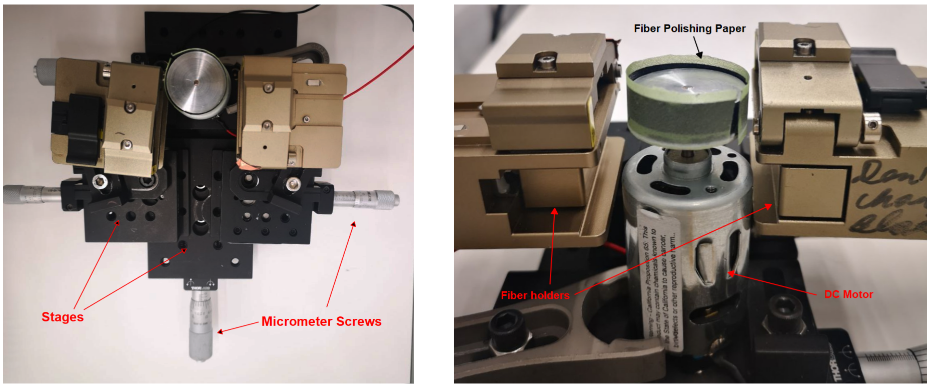

Figure 3.19: Set up used for the fiber lapping.

fiber positioning at the top of the external part of the probe is fabricated during the front-side dry etching of the release process. In order to comply with the device total thickness requirement, aimed at the minimization of the brain damages during insertion, this etching is performed up to $30\mu m$ from the top surface of the probe being the total thickness. Therefore, the groove aimed at the fiber positioning has the same depth.

3.5.3 Results: Fiber lapping

However, commercial optical fibers have a diameter of $125\mu m$ (cladding). In order correctly match the fiber into the groove a solution have been found: perform a lateral lapping of the fiber in order to reduce its diameter obtaining a D-shaped profile. Ahmad et. al. [57] in 2017 demonstrated a novel approach to realize lapped D-shaped single-mode fibers with insertion loss of $0.95dB$. Reproducing the set-up of the article cited before, the lapping mechanism is performed as following: several stages with micrometric screws, from *ThorLab*, have been assembled together

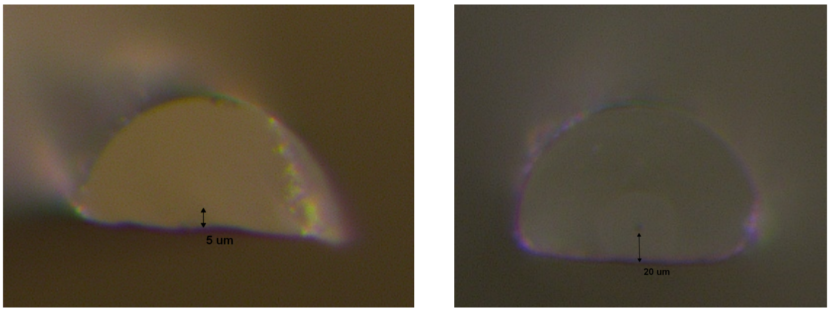

Figure 3.20: On the left an optical fiber lapped up to $5\mu m$ from the core, on the right lapped up to $20\mu m$.

in order to allow a precise two axes movement, as shown on left of fig. 3.19; two fiber cleaving tools have been exploited to clamp the fiber along the transversal axis, right of fig. 3.19; a DC Step motor, from *Mabuchi*, is placed at the center of the longitudinal axis, in which a metal cylinder, surrounded by *ThorLab* polishing paper [56], have been mounted on top.

This set-up allows to reduce the fiber diameter thanks to the lapping mechanism exploited with the rotating fiber polishing paper, ideally with micrometer precision thanks to the stages exploited. Moreover, the fiber can also be shifted in the transversal axis in order to perform the lapping along $2mm$, that is the length of the groove in the probe.

Since, as said before, the fiber are $125\mu m$ in diameter and the groove $30\mu m$ in depth, in order to allow a correct positioning around $90\mu m$ have to be removed. In this way positioning the fiber with the lapped side downwards, the fiber core will match the input waveguide allowing a good alignment. With the help of an optical microscope, to monitor the process, some lapping have

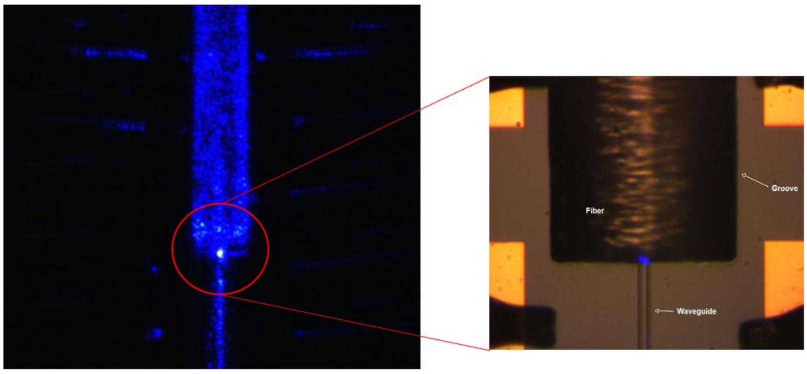

Figure 3.21: The fiber is aligned with the help of a micro-manipulator while the output power is measured, as shown in the left. Then it is fixed through an UV curable glue.

been performed in commercial Optical fiber. In figure 3.20 two example of lapping tests are shown. The fiber on the left have been lapped up to $5\mu m$, the right one $20\mu m$ from the core.

However, the fiber lapping process resulted to be not high controllable. The amount and the length of lapped fiber are still a critical point.

Once lapped, the fiber is handled with a micro-manipulator and aligned to the waveguide with a $637nm$ laser, as shown in fig. 3.21, during this step with the help of an optical microscope the output intensity is monitored. When the intensity is maximised, the glue is dispensed (UV curable glue) and re-alignment is performed in case of shifting then by directly exciting the fiber with a $405nm$ laser the glue is cured. Finally a second cure after 3 minutes exposing the glue with a UV gun id performed.

Then power measurement is performed, with a camera which has been calibrated with respect to the reading of a *ThorLab* optical powermeter. The average additional losses due to the fiber gluing process are $\simeq 13dB$, presenting strong variations $4.3-23dB$. The causes of this losses are difficult to be framed, since there are many variable parameters still not well controlled, such as the fiber-waveguide gap, the tilting of the fiber in the groove, and the already cited lapping process. Although the fiber lapping process seemed to be an easy and effective process to allow the insertion of the fiber in the limited groove depth, because of the high losses and low reproducibility obtained another approach is being investigated: HF (Hydrogen fluoride) fiber etching. It allows a good control and the possibility to perform the fiber diameter reduction in batch processes.

3.6 Electrode's impedance

As already discussed in 1.3.1, one of the major hurdle of the electrical read out system of silicon based neural probes is the impedance of each channel. Recently, the purpose of high density read-out, reduced device footprint and single neuron activity detection lead to the scaling down of the recording sites and consequently an increase of their impedance. Although, in order to achieve high Signal to Noise ratio the area of each pad has to be maximized. A solution have been found nanostructuring each electrode, through electroplating of black Platinum, as shown in fig. 3.22, and deposition techniques of novel materials as carbon based materials, thus obtaining a rough surface that provides a

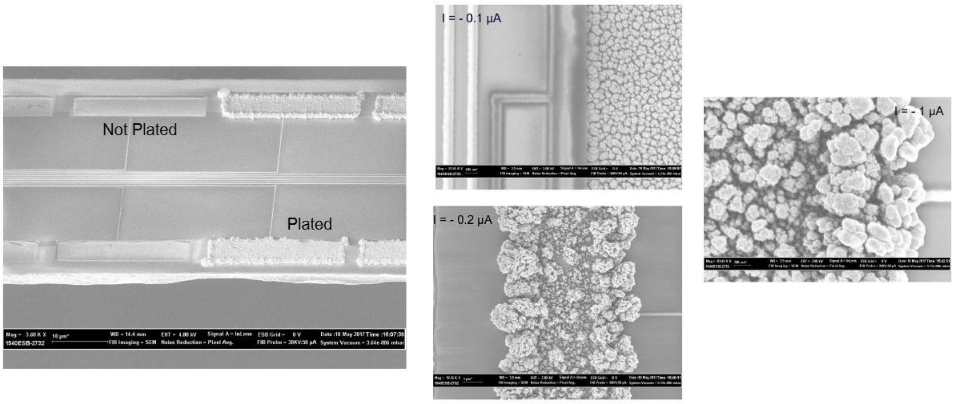

Figure 3.22: SEM pictures of the pads after Pt black electroplating, on the left. On the right zoom of different pads plated obtained at different currents showing different grain size.

wide effective area keeping the same dimensions.

The NanoZ® tool [58] can be plugged to the *Samtec* connectors on the top of the Printed Circuit Board and can control electrode arrays applying potentials, currents and reading the electrical impedance. This tool can be exploited to tests the channels, measuring their impedance in saline solution, and also to perform electroplating.

Impedance characterization in saline solution have been obtained showing an average of $4.5 \pm 0.1 M\Omega$ at $1kHz$ for each electrode [33]. Electroplating in a Black Platinum solution has been achieved using the NanoZ by applying a DC current to each current of $-0.1\mu A$ for $12s$. The impedance after the electroplating is on average $200 \pm 30k\Omega$.

3.7 Plating of novel materials: Carbon based materials

Carbon materials have been widely used for bioelectrochemical applications, they have been shown to display different morphological patterns and structural characteristics. These carbon based materials support microorganisms in mediating electron transfer reactions at high rates and they are considered to be the most promising group of electrode materials for bioelectrochemical applications. [59] Ranging from Activated Carbons (ACs) to Carbon Nanotubes (CNTs) these novel materials are the most widely used electrodes coatings because of their properties including low cost, ease of processability and controllable porosity. [60]

In this Thesis work the attention have been focused on the deposition of Activated Carbons (ACs) on electrodes recording sites. In particular ACs are the mostly used electrode materials, started to be studied for batteries and supercapacitors, due to their large surface area, good electrical properties and moderate cost. ACs are generally produces from physical and/or chemical activation of various kinds of carbonaceous materials (eg. wood, coal, etc.) Depending on their activation method and the precursors used, they have various physicochemical properties with very high surface area as high as $3000 m^2 g^{-1}$. In particular, ACs porous structure have a broad pore size distribution consisting of micropores ($< 2nm$), mesopores ($2 - 50nm$) and macropores ($> 50nm$). [60]

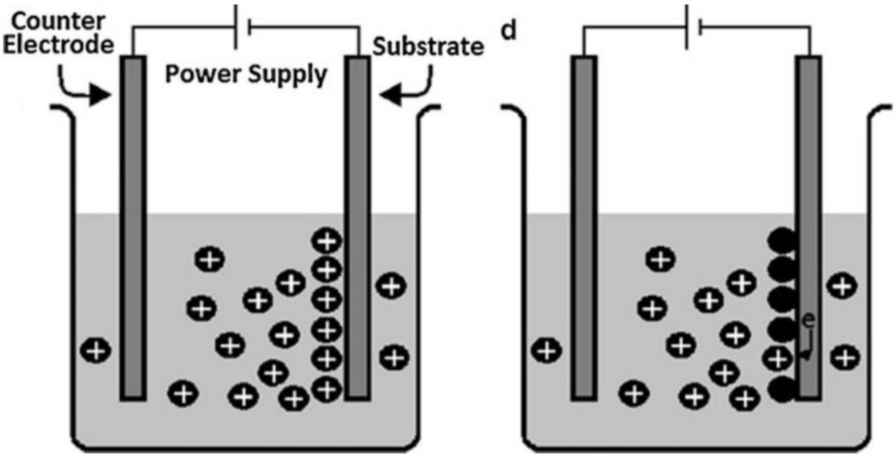

Figure 3.23: Scheme of EPD: on the left mechanism of Electrophoresis; on the right deposition. [61]

The high porosity and the high rate electron transfer could solve the high impedance electrodes issue, cited above, increasing the effective surface area of the recording sites in the shank of the probe.

3.7.1 Results: Deposition of Activated Carbon

In order to perform the deposition of ACs on the electrodes Electrophoretic Deposition (EPD) have been exploited. EPD is colloidal process where suspended particles in a stable solution are driven from the suspension medium to the substrate by an electric field. [61] A sketch of the mechanism is shown in fig. 3.23.

Pech et. al. in 2010 [62, 63] demonstrated the deposition of Onion-Like carbon as well as Activated Carbon on a gold patterned substrate applying a DC voltage of $50Vcm^{-1}$. The same colloidal solution of ACs have been prepared with 0.3 wt.% of Activated carbons in a $95\% - 5\%$ ethanol-water solution. Then in

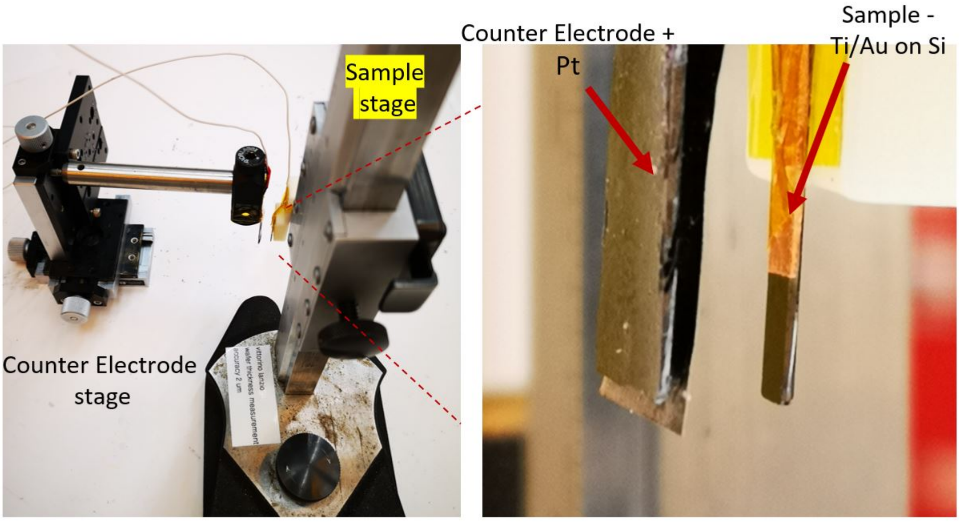

Figure 3.24: Setup exploited to perform Electrophoretic Deposition of Activated carbon on a Gold substrate.

order to stabilize the carbon particles 0.03 wt.% of $MgCl_2$ have been added to the suspension, since near the electrode under the effect of the electric field hydroxyl ions (OH^-) react with Mg^{2+} ions absorbed on the carbon particles to form $Mg(OH)_2$ that acts as an inorganic binder for the deposited particles. [64] The characterization of the solution prepared so far showed a conductivity $\sigma = 38\frac{\mu S}{cm}$, and a pH of 6.3 at 19° C. A setup containing two movable stages for the target sample and for the Platinum counter electrode, shown in fig. 3.24, has been built in order to control the distances between them, mainted constant at $0.5mm$. Preliminary deposition tests have been performed using the NanoZ® tool on probes wirebonded to the PCB. Exploiting a AC current of the order of μmA for 1 min and performing impedance measurements before and after the deposition. Results showed the impedance dropping from $3M\Omega$ to $100-400k\Omega$ at $1kHz$, demonstrating that the deposition of Activated Carbons and the increase of surface area was achievable. However, the EPD with the NanoZ® tool was not reproducible and well controllable, since in most case the lowest current reachable by the tool ($1\mu A$) caused an overdeposition of the material. In order to achieve a controllable process the approach have been changed, using a current generator and starting from a bigger gold coated sample to optimize the parameter for the electrodes deposition. Therefore, several test have been performed exploiting a Ti/Au on silicon substrate of $1cm^2$ of area, and using an DC current of $2mA$, through a current generator. However the deposition was not achieved, since rinsing the sample with ethanol no trace of Activated carbons were found on the surface. EPD with AC currents, with Duty Cycle $> 50\%$, were tested giving appreciable results. It can be explained because an alternated current allows, in the negative time period, to move back the unbounded particles and reactivate the gold surface, making the deposition more efficient. Therefore, EPD with AC current square waveform of $2mA$, Duty Cycle 70%, frequency $100Hz$, on the same kinf of sample, allows a stable deposition on the gold substrate, as shown in fig. 3.25.

The second step to optimize the deposition parameters have been to perform the EPD on electrodes of unused Printed Circuit Board (PCB) $\simeq 75\mu m \times 20\mu m$.

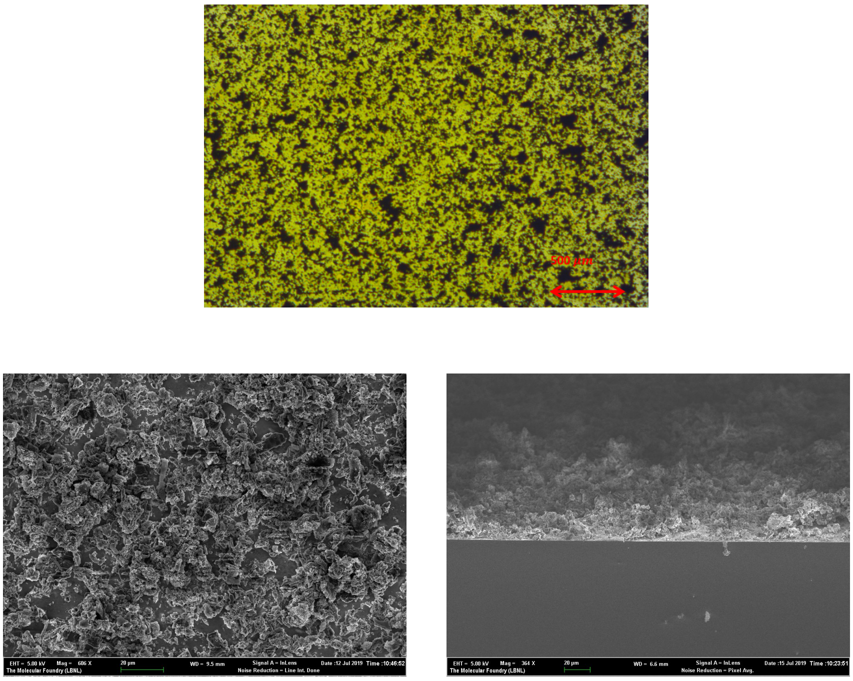

Figure 3.25: On the top an picture of the Ti/Au, $1cm^2$ sample after 10min of deposition. On the bottom SEM picture of the same sample, top view and cross section.

Here electrical characterizations have been done before and after the EPD step, performed with the current generator, in Saline solution with the NanoZ® tool, thanks to the possibility to connect the PCB to this tool through the *Samtec* connector. Deposition with $\simeq 10\mu A$ AC current for 1 minute. Impedance measurement in saline solution showed $100 - 300k\Omega$ at $1kHz$ before the EPD and $30 - 60k\Omega$ at $1kHz$ afterwards.

Once established the parameters for the deposition, EPD on the patterned electrodes have been performed.

The sample have been prepared fabricating the electrical system on a Si substrate and then passivating the wires with ALD oxide, with the same process steps of the complete fabrication.

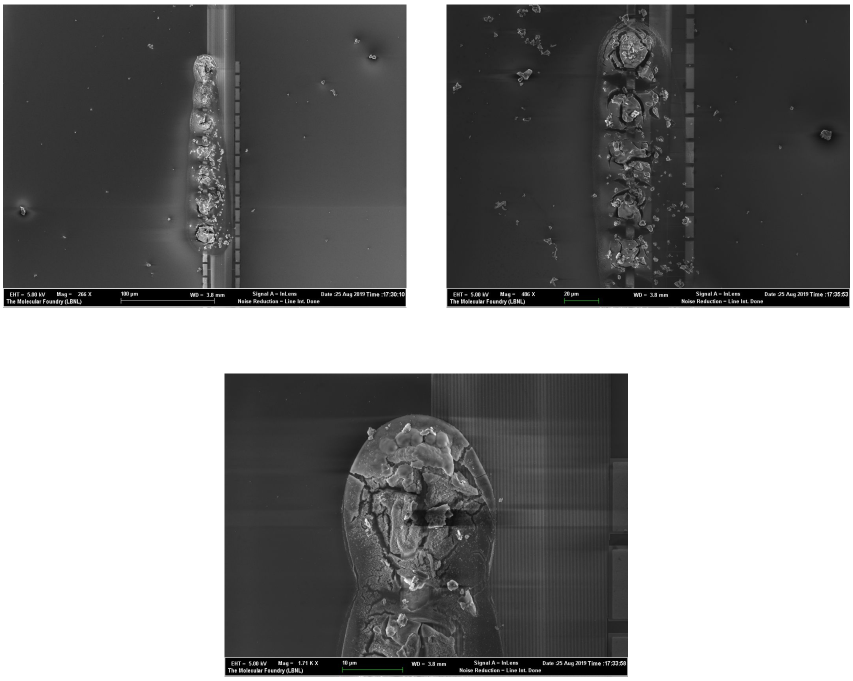

Figure 3.26: SEM pictures of EPD deposition on passivated electrodes in the probe shank. Selective depositions of Activated Carbons on electrodes have been performed. From the last pictures, showing a single one coated electrodes, contamination of the solution is present. The carbons are overdeposited short-circuiting the electrodes.

Since the surface area of the patterned electrodes $(5\mu \times 25\mu m)$ of the probe are smaller than the ones used before, a scale down of the parameters have been done and stable depositions have been found to be using an AC current square waveform in average of $0.6\frac{\mu A}{min}$, Duty Cycle 80%, frequency $100Hz$ per each electrode. In order to achieve this small value of current, since it was out of sensibility of the generator, the deposition was performed by parallelizing the electrodes and connecting them together to power supply. SEM characterization have been done, as shown in fig. 3.26, showing selected electrodes of the active part of the probe coated with Activated Carbon. In the surrounding of the electrodes it's evident a non investigated contamination of the solution with particles smaller than the ACs. Moreover, the Carbons seem to be in contact from one electrode to another probably making a electrical contact in between them. Therefore, the EPD for the electrodes has to be still optimized using lower deposition time or lower currents. Moreover, future works comprehend the deposition of other materials, with the same purpose of decreasing the electrode impedance and achieve high Signal to Noise ratio, as carbon based (Onion-like carbon [62]), or conductive polymers as PEDOT [65].

CHAPTER 4

Conclusions and Future Developments

In this Master Thesis project, the optimization of the design and the fabrication of the electrical layer, the etching processes, the electroplating of metal as well as carbon based material and the integration of the optical and electrical systems have been carried out. The final goal was to fabricate, through microelectonic technologies approaches at wafer scale, the first high density, multi-functional optoelectronic neural probe for locally monitoring and stimulating the central nervous system.

The work discussed in the previous chapters has been carried in collaboration with the Lawrence Berkeley National Laboratory, Molecular Foundry - Nanofabrication facility. The project proposes a micro-device able to simultaneously monitor and stimulate small population of neurons of the central nervous system of the brain cortex. The goal is achieved implementing and integrating two different circuits in the device: the electrical one for monitoring and the optical one for stimulation. The electrical circuit is composed of a set of 64 gold electrodes in both the external part of the probe, with the task of connection to external electrical control, and in the shank of the probe, which is the active part of the device that will be inserted in the brain. The shank electrodes have the task of interface nervous cells, sensing the Local Field Potentials generated by their electrical activity. On the other hand the optical circuit provides a certain number of rings resonators, waveguides and focusing gratings in order to stimulate genetically modified light-sensitive neurons above the gold electrodes. Once the neurons are stimulated, the electrodes will record the subsequent electrical activity.

The critical step encountered was the fabrication of the electrical system. The low working electrodes yield ($50 - 70\%$) and the presence of short circuits in between the wires ($15 - 30\%$) presented an issue for the performances of the recording task. Optimization of the pattern transfer in the exposure and development steps, through tests on the dose-sonication relation, the layout design critical for the formation of short circuits, and the lift-off process delicate for the dimensions of the wires lead to the achievement of good results. The working electrode yield has been increased to $96.85 - 100\%$, and the presence of short circuits reduced up to $5 - 10\%$. Further efforts are needed to achieve no shorts in between wires, indeed thanks to the algorithms exploited for the triangulation of the neurons, as discussed in the previous chapter, the electrode yield value could be considered satisfying for this application.

Another critical step encountered was the deposition of Activated Carbons (ACs) on the recording sites, with the purpose to increase the Signal To Noise ratio of the electrical read-out. Several tests in order to achieve good electrochemical parameters for a controllable deposition have been carried out. Results showed the possibility to selectively deposit the ACs on single electrodes, through Electrophoretic deposition, and to reduce their impedance. Further studies and optimization have to be carried to achieve a well controlled process.

Concerning, instead, the optical system optimizations of the etching process for the waveguides pattern transfer and the input optical fiber connection have been tried. Scattering losses due to the waveguides edge roughness use to limit the output optical power. Reactive Ion Etching recipe ($CHF_3 - O_2$) have been studied varying the relative gas concentrations and the pressure in the reaction chamber with the purpose of limiting the edge polymers formation and consequently the roughness without eliminating the soft mask employed. However, optical measurements did not show an increase of performances. Different approaches have to be investigated, as the use of an hard mask to remedy the resist thinning. The optical fiber, used as light input for the optical system, connection step have been investigated using a novel method

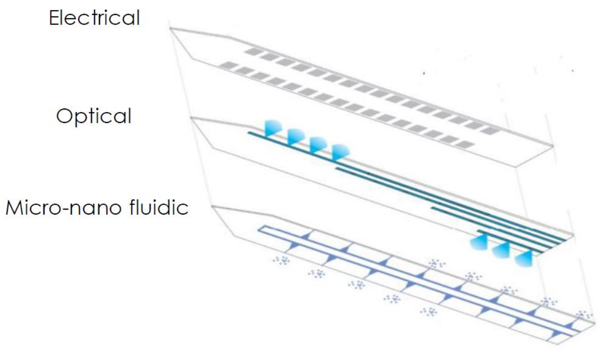

Figure 4.1: Possible new design of the probe integrating a MicroFluidic circuit.

consisting on the edge lapping to achieve a D-shape ending favorable to the match with device width, that is limited by the minimal brain damage requirement. The process showed low optical performances and low controllability , therefore the it should be optimized or moreover the fiber thinning goal should be achieved with different methods, as the etching in HF.

Finally, the stacked integration of the two circuits have been optimized employing a flowable oxide as planarization layer in between the optical and the electrical system. The process showed good results in term of ease of processability without lowering the electrical and optical performances of the probe.

To summarize, the optimization of the recipes have been able to release the neural probes ready to be sent to neuroscientists for *in-vivo* tests on rats, that will finally validate the performances and the limits of the device. After this thesis work, the neural probe project will proceed with the already cited development needed to push the performances, and with further multifunctionality as the implementation of microfluidic channels. The goal of this new component is the stimulation of the neural activity by a chemical point of view: the microfluidic channels will deliver the necessary ions to cause the release of neurotransmitters. A possible sketch is shown in fig. 4.1.

Once successful, the neural probe will help to go toward experiments in the human brain in order to give us as mush information as possible about the neural system itself, or in order to be used as Brain-Machine Iterface.

Bibliography

[1] R. L. Squire, F. E. Bloom, N. C. Spitzer, S. du Lach, A. Ghosh, and D. Berg. Fundamental Neuroscience. 3rd ed. Academic Press, 2008.

[2] R. Morris and M. Fillenz. Neuroscience: Science of the brain - An introduction for young students. 2003, p. 60.

[3] How to transfer a memory. 2018. url: http://www.visembryo.com/story4997.html.

[4] A. Scott. Neuroscience: A mathematical primer. Springer. Springer - Verlag New York, 2002. Chap. 2. Structure of a neuron

[5] D. Banks. Neurotechnology. In: Enginering Science and Educational Journal 3 (June 1998), pp. 135144.

[6] PhysiologyWeb at www.physiologyweb.com Copyright 2000-2019. Url:https://www.physiologyweb.com/lecture_notes /neuronal_action_potential_refractory_periods.html

[7] Thanapitak, Surachoke. (2012). Bionics Chemical Synapse. 10.13140/RG.2.1.2295.1288.

[8] The Open Neuron Project. URL: http://openneuronproject.org/synapse/

[9] World Health Organization. Global Health Estimates 2016 Summary Tables. Table April 2018 Url: https://www.who.int/healthinfo/global_burden_disease/ _Deaths_Global_2000_2016.xls?ua=1

[10] S. Waldert, T. Pistohl, C. Braun, T. Ball, A. Aertsen, and C. Mehring, A review on directional information in neural signals for brain-machine interfaces, J. Physiol. Paris, 2009.

[11] S. Waldert, Invasive vs. non-invasive neuronal signals for brain-machine interfaces: Will one prevail?, Front. Neurosci., vol. 10, no. JUN, pp. 14, 2016.

[12] K. D.Wise, J. B. Angell, and A. Starr. An Integrated Circuit Approach to Extracellular Microelectrodes. In: IEEE Transactions on Biomedical Engineering BME-17.3 (July 1970)

[13] Z. Fekete, Recent advances in silicon-based neural microelectrodes and microsystems: A review, Sensors Actuators, B Chem., vol. 215, pp. 300315, 2015.

[14] Rousche P.J.; Pellinen D.S.; Pivin D.P.; Williams J.C.; Vetter R.J.; Kipke D.R. Flexible polyimide-based intracortical electrode arrays with bioactive capability. In: IEEE Trans. Biomed. Eng. (2001, 48, 361-371.).

[15] Metz S.; Bertsch A.; Bertrand D.; Renaud P. Flexible polyimide probes with microelectrodes and embedded microfluidic channels for simultaneous drug delivery and multi-channel monitoring of bioelectric activityv. In: Biosens. Bioelectron. (2004, 19, 1309-1318.).

[16] Stieglitz T. Flexible biomedical microdevices with double-sided electrode arrangements for neural applications. In: Sens. Actuat. A-Phys. (2001, 90, 203- 211.).

[17] Stieglitz T.; Gross M. Flexible BIOMEMS with electrode arrangements on front and back side as key component in neural prostheses and biohybrid systems. In: Sens. Actuat. B-Chem (2002, 83, 8-14.).

[18] R. Bhandari, S. Negi, F. Solzbacher, Wafer-scale fabrication of penetrating neural microelectrode arrays, Biomed. Microdevices 12 (2010) 797.

[19] P. Norlin, M. Kindlundh, A. Mouroux, K. Yoshida, and G. U. Hofmann. A 32-site neural recording probe fabricated by DRIE of SOI substrates. In: Journal of Micromechanics and Microengineering 12.4 (June 2002), pp. 414419.

[20] Stevenson, I. H. & Kording, K. P. How advances in neural recording affect data analysis. Nat. Neurosci. 14, 139142 (2011)

[21] G. Hong and C. M. Lieber, Novel electrode technologies for neural recordings, Nat. Rev. Neurosci., vol. 20, no. June, pp. 330345, 2019.

[22] I. Cho, H. Won Back, and E. Yoon. A 16-site neural probe integrated with a waveguide for optical stimulation. In: IEEE 23rd International Conference on Micro Electro Mechanical Systems (MEMS) (2010), pp. 995998.

[23] C. A. R. Chapman, N. Goshi, and E. Seker, Multifunctional Neural Interfaces for Closed-Loop Control of Neural Activity, Adv. Funct. Mater., vol. 28, no. 12, pp. 130, 2018.

[24] Y. Li, K. Baek, M. Gulari, and K. D. Wise. A Drug-Delivery probe with an in-line flowmeter based on trench refill and chemical mechanical polishing techniques. In: Sensors, 2007 IEEE (2007), pp. 11441147.

[25] D. Papageorgiou, S. C. Bledsoe, M. Gulari, J. F. Hetke, D. J. Anderson, and K. D. Wise. A shuttered probe with in-line flowmeters for chronic in-vivo drug delivery. In: Technical Digest. MEMS 2001. 14th IEEE International Conference on Micro Electro Mechanical Systems 01CH37090 (2001), pp. 212215.

[26] M. Scanziani and M. Hausser. Electrophysiology in the age of light. In: Nature 461.3 (Oct. 2009), pp. 930939.

[27] G. R. Sune. Electron Beam Litography for Nanofabrication. Ph.D. Thesis. Universitat Autonoma de Barcelona, 2008.

[28] P. Naulleau. Optical Lithography. In: California digital library. Lawrence Berkeley National Laboratory (Apr. 2014).

[29] A. P. Nayak and M. Logeeswaran VJ. andn Saif Islam. Wet Etching. In: Encyclopedia of Nanotechnology (2012). Ed. by Bushan B.

[30] A. P. Nayak and M. S. Logeeswaran VJ. andn Islam. Dry Etching. In: Encyclopedia of Nanotechnology. Springer (2012). Ed. by Bushan B.

[31] A. M. Lieberman and A. J. Lichtenberg. Principles of Plasma Discharges and Materials Processing. 2nd ed. Wiley - Interscience. John Wiley e Sons, 2005.

[32] M. Ritala and M. Leskela. Chapter 2 - Atomic Layer Deposition. In: Handbook of Thin Films 1: Deposition and Processing of thin films (2002). Ed. by H.S Nalwa, pp. 103159.

[33] V. Lanzio et al., High-density electrical and optical probes for neural readout and light focusing in deep brain tissue, J. Micro/Nanolithography, MEMS, MOEMS, vol. 17, no. 02, p. 1, 2018.

[34] G. Nagel, T. Szellas, W. Huhn, S. Kateriya, N. Adeishvili, P. Berthold, D. Ollig, P. Hegemann, and E. Bamberg. Channelrhodopsin-2, a directly light-gated cation-selective

membrane channel. In: PNAS 100.24 (Nov. 2003), pp. 13940 13945.

[35] C. Palmer and E. Loewen. Diffraction Grating Handbook. 6th ed. Newport corporation, 2005.

[36] A. Katzir, A. C. Livanos, and A. Yariv, Chirpedgrating output couplers in dielectric waveguides, Appl. Phys. Lett., vol. 30, no. 5, pp. 225226, Mar. 1977.

[37] M Megas, Zs Emri, T.F Freund, A.I Gulys, Total number and distribution of inhibitory and excitatory synapses on hippocampal CA1 pyramidal cells, Neuroscience, Volume 102, Issue 3, 2001, Pages 527-540, ISSN 0306-4522,

[38] A. Leinse, Shaoxian Zhang, and R. Heideman, TriPleX: The versatile silicon nitride waveguide platform, pp. 6767, 2016.

[39] Roeloffzen, C. G. H., Hoekman, M., Klein, E. J., Wevers, L. S., Timens, R. B., Marchenko, D., Boller, K. J. (2018). Low-loss si3n4 triplex optical waveguides: Technology and applications overview. IEEE Journal of Selected Topics in Quantum Electronics, 24(4).

[40] Ji, X., Barbosa, F. A. S., Roberts, S. P., Dutt, A., Cardenas, J., Okawachi, Y., Lipson, M. (2016). Breaking the Loss Limitation of On-chip High-confinement Resonators.

[41] Ji, X., Barbosa, F. A. S., Roberts, S. P., Dutt, A., Cardenas, J., Okawachi, Y., Lipson, M. (2017). Ultra-low-loss on-chip

resonators with sub-milliwatt parametric oscillation threshold. Optica, 4(6), 619.

[42] Roberts, S. P., Ji, X., Cardenas, J., Bryant, A., & Lipson, M. (2017). Sidewall Roughness in Si3N4 Waveguides Directly Measured by Atomic Force Microscopy. 1(d), SM3K.6.

[43] Jansen, H., Gardeniers, H., De Boer, M., Elwenspoek, M., & Fluitman, J. (1996). A survey on the reactive ion etching of silicon in microtechnology. Journal of Micromechanics and Microengineering, 6(1), 1428.

[44] ZEP520A, Technical report. Url: http://www.nanophys.kth.se/nanophys/facilities/nfl/resists/zep520a-7-2.pdf

[45] Remover PG, Data sheet. Url: http://www.nano.pitt.edu/sites/default/files/MSDS/Developers/Remover%20PG.pdf

[46] S.P. Jeng, et al., in: Proceeding of VLSI Symposium, Kyoto, Japan, 1995, pp. 1521.

[47] H. C. Liou and J. Pretzer, Effect of curing temperature on the mechanical properties of hydrogen silsesquioxane thin films, Thin Solid Films, vol. 335, no. 12, pp. 186191, 1998.

[48] C. W. Holzwarth, T. Barwicz, and H. I. Smith, Optimization of hydrogen silsesquioxane for photonic applications, J. Vac.

Sci. Technol. B Microelectron. Nanom. Struct., vol. 25, no. 6, p. 2658, 2007.

[49] Application of flowable oxides in photonics, Mater. Sci. Pol., vol. 26, no. 1, pp. 189194, 2008.

[50] K. L. Lee, J. Bucchignano, J. Gelorme, and R. Viswanathan, "Ultrasonic and dip resist development processes for 50 nm device fabrication" Journal of Vacuum Science & Technology B: Microelectronics and Nanometer Structures Processing, Measurement, and Phenomena 15, 2621 (1997);

[51] Z. Cui, "Nanofabrication: Principles, Capabilities and Limits", 2009, Springer US

[52] Microchemicals GmbH. Thick Resist Processing. Application notes. 2013.

[53] Advanced MicroMachined Tools, Single Ow Wafer Holder. Copyrights 1997-2019 AMMT GmbH. All Rights reserved. Url: https://www.ammt.com/products/wet-etching/single-series/

[54] KOH Etching, BYU Cleanroom. URL: https://cleanroom.byu.edu/KOH

[55] ProTeck B3 datasheet: https://www.seas.upenn.edu/ nanosop/ documents/ds_protek_b3.pdf

[56] ThorLabs, LF30D - 6" x 6" Diamond Lapping (Polishing) Sheets, 30 m Grit (5 Sheets). Url:

https://www.thorlabs.com/thorproduct.cfm?partnumber =LF30D

[57] H. Ahmad, H. A., I. S. Amiri, I. S. A., A. Z. Zulkifli, A. Z. Z., H. Hassan, H. H., R. Safaei, R. S., & and K. Thambiratnam, and K. T. (2017). Stable dual-wavelength erbium-doped fiber laser using novel fabricated side-polished arc-shaped fiber with deposited ZnO nanoparticles. Chinese Optics Letters, 15(1), 011403011407.

[58] NanoZ, Impedance Testing for In Vivo probes. Url: https://www.multichannelsystems.com/sites/ multichannelsystems.com/files/documents/brochures/nanoZ-Brochure.pdf

[59] Rathinam, N. K., Salem, D. R., & Sani, R. K. (2019). Biofilm Engineering for Improving the Performance of Microbial Electrochemical Technologies. Microbial Electrochemical Technology, 315338.

[60] Zhang, L. L., & Zhao, X. S. (2009). Carbon-based materials as supercapacitor electrodes. Chemical Society Reviews, 38(9), 25202531.

[61] Structures, N. M. (2015). Handbook of Nanoelectrochemistry. Handbook of Nanoelectrochemistry, (June).

[62] Nagel, G., Ollig, D., Fuhrmann, M., Kateriya, S., Musti, A. M., Bamberg, E., & Hegemann, P. (2002). Channelrhodopsin-

1: A light-gated proton channel in green algae. Science, 296(5577), 23952398.

[63] Pech, D., Brunet, M., Durou, H., Huang, P., Mochalin, V., Gogotsi, Y., Simon, P. (2010). Ultrahigh-power micrometre-sized supercapacitors based on onion-like carbon. Nature Nanotechnology, 5(9), 651654.

[64] Russ, B. E., & Talbot, J. B. (1998). An analysis of the binder formation in electrophoretic deposition. Journal of the Electrochemical Society, 145(4), 12531256.

[65] Groenendaal, L.; Jonas, F.; Freitag, D.; Pielartzik, H.; Reynolds, J. R. (2000). "Poly(3,4-ethylenedioxythiophene) and Its Derivatives: Past, Present, and Future". Advanced Materials. 12 (7): 481494.